IEEE Access
Multidisciplinary | Rapid Review | Open Access Journal

Date of publication xxxx 00, 0000, date of current version xxxx 00, 0000.

Digital Object Identifier 10.1109/ACCESS.2017.DOI

Skin Conductance Response Artifact Reduction: Leveraging Accelerometer Noise Reference and Deep Breath Detection

MD RAFIUL AMIN[1], (Member, IEEE), SAMIUL ALAM[1], SAMAN KHAZAEI[1,3], HAMID FEKRI AZGOMI[1,2], and ROSE T. FAGHIH[1,3], (Senior Member, IEEE)

[1]Department of Electrical and Computer Engineering, University Of Houston, Houston, Texas (e-mail: mamin@uh.edu, salam@uh.edu)
[2]Department of Neurological Surgery, the University of California, San Francisco, CA (e-mail: hfekriaz@uh.edu)
[3]Department of Biomedical Engineering at New York University, New York City, NY (email: sksk9861@nyu.edu, rfaghih@nyu.edu)

Corresponding author: Rose T. Faghih (e-mail: rfaghih@nyu.edu).

This work was supported in part by NSF grant 1942585/2226123 - CAREER: MINDWATCH: Multimodal Intelligent Noninvasive brain state Decoder for Wearable AdapTive Closed-loop arcHitectures and 1755780 - CRII: CPS: Wearable-Machine Interface Architectures and New York University Faculty Startup Fund.

ABSTRACT *Goal:* Electrodermal activity (EDA) shows a significant correlation with activation of the autonomic nervous system (ANS) activation. Regular ambulatory monitoring via wearables and consequent inference of ANS activation has a wide range of applications tracking mental health. The real-world implementation of a closed-loop system to regulate one's emotional state to improve their mental well-being requires an accurate and reliable estimation of ANS activation in ambulatory settings. *Challenge:* However, the presence of motion artifacts in skin conductance (SC) data collected in ambulatory settings makes the analysis for such estimation unreliable. *Methods:* We propose a multi-rate adaptive filtering scheme to reduce motion artifacts in SC data that utilizes three-axis accelerometer data. We investigate four types of linear and nonlinear adaptive filters. We use both simulated and experimental data to investigate the performance of adaptive filters. Furthermore, we utilize the respiration signal to identify the probability of respiration-induced SC artifacts. Next, we use a Bayesian filter-based deconvolution approach to identify SC responses (SCRs) induced by underlying arousal events and deep breaths. Finally, we propose to use the respiration signal to separate the artifacts in SC due to deep breaths. *Results:* Our results show that linear finite impulse response least squares recursive filters perform best among the four types of adaptive filters studied. We draw this conclusion by obtaining receiver operating characteristics of event-related SCRs detection with deconvolution after artifact reduction with different adaptive filters. Moreover, for all of our simulated and experimental datasets investigated in this study, we observe that the recursive least-squares filter always provides stable results. Additionally, our results show our ability to detect respiration-induced SCRs and the corresponding activation of ANS. *Conclusion:* The evaluation of adaptive filters shows the potential to utilize reference signals for successful artifact modeling and reduction. *Significance:* Effective artifact reduction will lead to reliable ANS activation monitoring and consequent robust implementation of a closed-loop wearable machine interface architecture to eventually improve one's mental health.

INDEX TERMS Active noise reduction, adaptive filters, biomedical signal processing, wearable sensors, electrodermal activity

I. INTRODUCTION

The phrase "electrodermal activity" (EDA) was introduced in 1966 to designate any electrical activity that is electrically measurable from the skin [1], [2]. Since its first observation in the 1880s [2], EDA has been widely used in physiology and psychophysiology studies as the information it contains has a relationship with the activation of the sympathetic nervous system (SNS) [3], [4]. SNS–a part of the autonomic nervous system (ANS)–is responsible for the fight-or-flight response mechanism in response to a stimulus

that the human brain categorizes as a threat to survival. When such an emotional stress stimulus is perceived, the brain stimulates the sweat glands via ANS, depending on the psychological and physiological demands. The subsequent secretion of salty sweat glands increases skin conductance (SC)–a measure of EDA–by increasing the number of electrical charge carrier ions. SC measurements contain rich information on SNS activation. Therefore, evaluating SC response (SCR) due to ANS activation will lead to more effective monitoring of emotional arousal fluctuations [5].

Efficient EDA analysis along with SNS activation inference have a wide range of applications, including detection of major depression [6], pain detection [7], tracking of cognitive stress [5], tracking of wakefulness [8], etc. Furthermore, abnormal regulation of EDA appears to be a reliable feature of depression and a potential marker of suicidal risk measurement [9]. Azgomi et al. [10] proposed a closed-loop wearable-machine interface architecture to regulate emotional arousal that utilizes EDA as observation. The proposed method comprises the identification of ANS activation using EDA deconvolution [11]–[13], the estimation of emotional stress [5], [14], [15], and finally closing the loop [16] to maintain the corresponding emotional state within the desired range. However, in ambulatory settings, recordings can have artifacts due to motion or other noise sources. For effective implementation of such a closed-loop regulation scheme, artifact reduction is a prerequisite.

The non-invasive nature of many biomedical sensors has led to many measurement technologies for ambulatory health monitoring. The most popular modality of biomedical sensors that are currently being deployed in many consumer devices along with wearable devices includes cardiac sensors e.g. electrocardiogram (ECG) electrodes and photoplethysmogram (PPG) optodes, skin temperature (SKT) sensors, muscle activity sensors e.g. electromyogram (EMG) electrodes, etc. [17], [18]. In addition, many low-power inertial sensors, such as accelerometers, gyroscopes, and magnetometers, are deployed in wearable devices to monitor user activity [19]. In the past few decades, numerous research efforts have led to the successful implementation of PPG signal analysis for wearable implementation, with the goal of continuous monitoring of cardiac health. This effort has led to applications ranging from daily heart rate monitoring [20] to efficient detection of atrial fibrillation to prevent heart stroke [21]. As motion can corrupt PPG signal recordings, to try to make day-to-day monitoring successful, many researchers worked on the prerequisite signal processing pipelines for motion artifact removal [21]. In other contexts, there are many studies proposing various signal processing techniques to remove motion artifacts from other biomedical signals such as ECG [22], [23], electroencephalogram (EEG) [24], functional near-infrared spectroscopy (fNIRS), etc. The motion artifact removal schemes are not only important for deploying sensors in consumer devices, but also it has been an important preprocessing pipeline for scientific research. Among popular approaches, motion reference based on inertial sensor measurements has been widely utilized to monitor activity.

If a possible noise source reference is available, adaptive filtering is one of the most desirable techniques for reducing the noise from the target signal [25]. Adaptive filters have been extensively studied to remove motion artifacts from various biomedical signals, including ECG [22], [23], PPG [26], [27], EEG [28], [29], fNIRS [30]. LMS (Least Mean Squares) filters are widely used in various biomedical signal processing applications, including ECG denoising, EEG signal enhancement [31]–[33]. These filters are known for their simplicity and adaptability, making them suitable candidates for motion artifact removal. RLS (Recursive Least Squares) filters have been extensively explored in biomedical signal processing due to their ability to adapt quickly to changing signal conditions. They have found applications in PPG noise cancellation [34], EEG noise cancellation [35], highlighting their relevance in the context of biomedical signal analysis. Volterra LMS and Volterra LMS filters are less common than LMS and RLS in biomedical signal processing, they have been employed in nonlinear system identification and modeling [36]. They may find relevance in signal analysis when dealing with nonlinear artifacts or complex relationships within the signal. However, to the best of our knowledge, there have not been studies that evaluate adaptive filters for the removal of motion artifacts from EDA utilizing reference information from inertial sensors. Although EDA is one of the most potential candidates for next-generation wearable health monitoring [37], the amount of research conducted on EDA signals to obtain information reliably is relatively limited compared to cardiac signals. In particular, very little research has been carried out to reduce the artifacts in EDA. There are a few studies that investigate different methods for artifact detection, including semi-supervised machine learning approaches [38] and unsupervised machine learning approaches [39], [40]. Moreover, supervised machine learning-based [41], deep auto-encoder-based [42], and wavelet-based heuristic [43] techniques are investigated to correct artifacts. However, those have not investigated noise reference information to model the artifact. Whether the motion artifacts can be represented as the linear or nonlinear transformation of a noise source reference (such as the accelerometer recording), and whether such transformation can be modeled with adaptive filters, are yet to be investigated. Furthermore, some of the fluctuations present in SC are related to respiration and may not be directly related to ANS activation. In 2003, Schneider et al. [44] reported evidence of misinterpretation of experimental observations due to irregular respiration-related SC activation. Hence, they proposed a rule-based approach to identify such cases. Later in 2019, Lee *et al.* [45] utilized a similar rule-based approach to detect and later remove respiration-related noise from SC data based on the PPG-derived respiration reference signal. However, a more systematic approach is required to identify and isolate such activations which can be referred to as respiration-induced noise.

Therefore, in this study, we evaluate linear adaptive filters as well as non-linear Volterra adaptive filters that take the three accelerometers as the reference signal to model the artifacts in a multi-rate manner as shown in Figure 1. We utilize a publicly available dataset and simulated artifacts to evaluate four types of adaptive filters. Furthermore, we perform experiments to induce motion artifacts during SC data collection while recording motion information with a three-axis accelerometer sensor. We evaluate the adaptive filtering performance of removing motion artifacts utilizing the experimental data. We also collect respiration reference signals to identify respiration-induced noise.

In the following sections, we first discuss the materials and methods which includes the experimentation for data collection, additional publicly available dataset description, mathematical basis adaptive filters, linear/nonlinear/multirate adaptive filters, the deconvolution algorithm for EDA [46], and proposed respiration removal technique. Finally, we present the results, discussions on the results, and conclusions.

1) Simulated Data

In addition to the experimental dataset that we collected, we also generated and analyzed a simulated dataset. This was done by taking the publicly available experimental dataset of SCRs to loud sounds [47] and adding known simulated artifacts to it. Bach *et al.* [4] designed this experiment to model event-related SCRs. The dataset includes SC data measurement from the thenar/hypothenar of the nondominant hand, the middle phalanx of the dominant second and third finger, and the medial plantar surface of the nondominant foot for each of the 26 participants. Here, we only utilize the SC recordings from the thenar/hypothenar of the non-dominant hand of all the participants for single-channel analysis. The details of the experiments and the dataset are provided in [4].

A. ADAPTIVE FILTERS

1) Wiener Filter

We briefly discuss the basics of adaptive filters that we use to evaluate artifact removal performance. In this study, we limit our scope to the adaptive filters *finite impulse response* (FIR). First, we describe the ideal case of filtering, and then we derive different adaptive filters with appropriate assumptions for practical implementation. The ideal case is known as *Wiener Filter* (WF). A WF has two inputs, a desired signal $d[k]$ and a noise reference signal $n[k']$ [25]. Here, we extend our assumption that $d[k]$ and $n[k']$ can have different sampling frequencies for multirate formulation. Furthermore, we extend our assumption here that the sampling frequency of the noise source $n[k']$ is higher than the desired signal $d[k]$. Let the sampling frequencies be F_d and F_n, respectively. We also assume that the sampling ratio $M = F_n/F_d$ is an integer. If the filter at k^{th} is defined with the vector $w[k]$ where $w[k, k']$ is the k'^{th} element in the filter at the k^{th} time step, then the filter output $z[k]$ can be written as

$$z[k] = w[k]^\top x[k],$$

where $x[k] = [\, n[Mk - L + 1]\ n[Mk - L + 2]\ \cdots\ n[Mk - 1]\ n[Mk]\,]^\top$. Here, L is the length of the FIR filter. The error vector can be represented as

$$e[k] = d[k] - z[k]. \tag{1}$$

The objective function for the WF algorithm is usually derived from the mean square error (MSE), which is represented as

$$\begin{aligned} J_w &= \mathbb{E}\{(e^2[k])\} \\ &= \mathbb{E}\{(d[k] - z[k])^\top (d[k] - z[k])\} \\ &= \mathbb{E}\{(d^2[k]\} - 2w[k]^\top \mathbb{E}\{d[k]x[k]\} \\ &\qquad + w[k]^\top \mathbb{E}\{x[k]x[k]^\top\} w[k]) \\ &= \mathbb{E}\{(d^2[k])\} - 2w[k]^\top p[k] + w[k]^\top R[k] w[k], \end{aligned} \tag{2}$$

where $p[k]$, and $R[k]$ represent the cross-correlation $\mathbb{E}\{d[k]x[k]\}$ and the autocorrelation of $\mathbb{E}\{x[k]^\top x[k]\}$, respectively. For WF, $w[k]$, $p[k]$, and $R[k]$ are considered constant for all k time points with the assumption that $d[k]$ and $x[k]$ are jointly wide-sense stationary (WSS). Therefore, the sample index k can be removed for the case of WF and can be written as w, p, and R. To minimize MSE, we need to find the minima of the function in (2). Therefore, we take the derivative with respect to w and set it to zero to obtain the optimal filter coefficient vector w_o.

$$\begin{aligned} \nabla_w J_w &= -2p + 2Rw = 0 \\ \Rightarrow w_o &= R^{-1} p. \end{aligned} \tag{3}$$

However, in practical settings, R and p are not known. Therefore, some approximation or good estimates of R and p are required. Mostly, different approximations of these leads to different types of adaptive filters, which we will discuss in later sections.

2) Least mean squares (LMS) Adaptive Filter

At the k^{th} step of least mean square (LMS) filter, the approximations are carried out as

$$\begin{aligned} \hat{R}[k] &= x[k]x[k]^\top, \\ \hat{p}[k] &= d[k]x[k]. \end{aligned}$$

We plug these approximations into (2) to obtain the approximation of MSE for the k^{th} sample as

$$\hat{J}_w[k] = d^2[k] - 2w[k]\hat{p}[k] + w[k]^\top \hat{R}[k] w[k].$$

We insert these approximations into (2) to obtain the approximation of MSE, J_w. Using this, the filter update equation for the k^{th} time stamp is as

$$w[k+1] = w[k] - \alpha \nabla_w \hat{J}_w[k], \tag{4}$$

where α corresponds to the step size. After simplification, the final equation becomes

$$w[k+1] = w[k] + \alpha e[k] x[k]. \tag{5}$$

3) Recursive Least Square (RLS) Adaptive Filter

At k^{th} step of recursive least square (RLS) filter, the approximations are carried out as

$$\hat{R}[k] = \sum_{i=0}^{k} \gamma^{(k-i)} x[i]x[i]^\top,$$
$$\hat{p}[k] = \sum_{i=0}^{k} \gamma^{(k-i)} d[k]x[k],$$

where γ is called the forgetting factor and is selected between $0 \leq \gamma \leq 1$. If we set $\gamma = 0$, then the corresponding RLS filters are the same as the LMS filter. We insert (2) to obtain the approximate MSE, J_w.

$$\hat{J}_w[k] = d^2[k] - 2w[k]\hat{p}[k] + w[k]^\top \hat{R}[k]w[k].$$

We set the derivative $\nabla_{w[k]} \hat{J}_w[k] = 0$ and find that the filter update equation for k^{th} is as,

$$w[k] = \hat{R}^{-1}[k]\hat{p}[k]. \tag{6}$$

However, this equation is computationally expensive. An iterative update can be performed using the weights calculated in the last step. After simplification, the update equation can be written as follows [25],

$$w[k+1] = w[k] + e[k]S_D[k]x[k], \tag{7}$$

where

$$\boldsymbol{\psi}[k] = S_D[k-1]x[k],$$
$$\boldsymbol{\phi}[k] = \frac{\boldsymbol{\psi}[k]}{\lambda + \boldsymbol{\psi}[k]},$$
$$S_D[k] = \frac{1}{\lambda}\left[S_D[k-1] - \boldsymbol{\psi}[k]\boldsymbol{\phi}[k]^T\right].$$

During initialization, set $S_D(0) = \delta\mathbb{I}$ where δ can be the inverse of an estimate of the input signal power; $x(0) = w(0) = [0\ 0 \cdots 0]$, and evaluate.

4) Second Order Volterra Adaptive Filters (LMS and RLS)

To obtain an n^{th} order Volterra LMS/RLS filter, we simply populate the reference signal vector with the nonlinear terms for each iteration and update the length of the adaptive filter coefficient vector accordingly. For example, for the 2^{nd} order case, the reference signal is

$$x[k] = [x_{\text{L}}[k]^\top\ x_{\text{NL}}[k]^\top]^\top$$
$$\text{where, } x_{\text{L}}[k] = [\,n[Mk-L+1]\ n[Mk-L+2]\ \cdots\ n[Mk]\,]^\top,$$
$$x_{\text{NL}}[k] = vec(x_{\text{L}}[k]x_{\text{L}}[k]^\top).$$

Here, 'vec' denotes the matrix-to-vector conversion operation. Now the corresponding adaptive filter length is $L' = L + L^2$, i.e., there are L' numbers of elements in the vector $w[k]$ for each time step. All other steps of the adaptive filter are the same as in the linear cases. We define $V2-LMS$ and $V2-RLS$ to refer to 2^{nd} order Volterra RLS and LMS filter.

B. ARTIFACT REDUCTION FROM SC SIGNAL WITH ACCELEROMETER NOISE REFERENCE

A part of the artifact contamination on SC signal is related to the movement of the sensors. Motion information can be recorded in many different forms. One of the popular ways is to utilize a three-axis accelerometer to measure the acceleration. A three-axis accelerometer records data for three different axes. Therefore, we have three different noise reference channels corresponding to three axes. For the discretized recordings, we combine the sample stream from these three signals into one discretized sample stream. Now, the new stream has a frequency that is three times the sampling frequency for the single channel. We perform an adaptive filter in the recorded SC signal, while considering the accelerometer recording as the noise reference. The SC signal, denoted as $y_{SC}(t)$, contains a DC component and some very low frequency components acting as a baseline. We remove these baseline low frequency components so that the mean value of the desired signal is zero. We consider the desired signal as the high pass version of the recorded raw SC signal. We perform low pass filter on the raw SC signal to obtain the slow varying component $y_{SCL}(t)$. Then we subtract the low pass filtered signal from the raw signal to obtain the high pass filtered SC signal, which is our desired signal $d[k]$. The noise reference $n[k] = [n_1[k-L+1]\ \ n_2[k-L+1]\ \ n_3[k-L+1]\ \ n_1[k-L+2]\ \ n_2[k-L+2]\ \ n_3[k-L+2]\ \ \cdots\ \ n_1[k]\ \ n_2[k]\ \ n_3[k]]$ and set $F_x = 3 \times F_d$ to perform the multi-resolution linear/nonlinear adaptive filtering. Here F_n corresponds to the sampling frequency of the combined noise reference, $n_i[k]$ represent the k^{th} sample of the accelerometer recording for the i^{th} channel representing a spatial axis, $\forall i \in \{1, 2, 3\}$. Before, combining all the accelerometer data into one noise vector, we perform a third order moving median filtering to remove any spike or outlier noise that has been observed in some of the accelerometer channel data. This noise does not represent motion artifacts and could be related to the internal electronics of the accelerometer. We perform the motion artifact removal on the signal at 100 Hz sampling frequency for $y_{SC}[k]$. Figure 1 shows an overview of the motion artifact removal scheme. If each channel of noise reference is uncorrelated then, it is trivial to show that this implementation is equivalent to multi-reference adaptive filters [48]. In a cascaded multi-reference filter, in every stage, the goal is to orthogonalize the error with respect to the corresponding noise reference vector. The later stage is then trained on the error from the previous stage same way. Therefore, the final error is orthogonal to all the reference vectors. In the proposed, architecture we represent this in a multi-rate formulation, where we find the final orthogonal residual error simultaneously for each of all noise references.

C. BAYESIANEDA FOR DECONVOLUTION OF SC RESPONSE

For obtaining the ANS from the SC signal, we take a deconvolution approach provided in [46]. We use the following

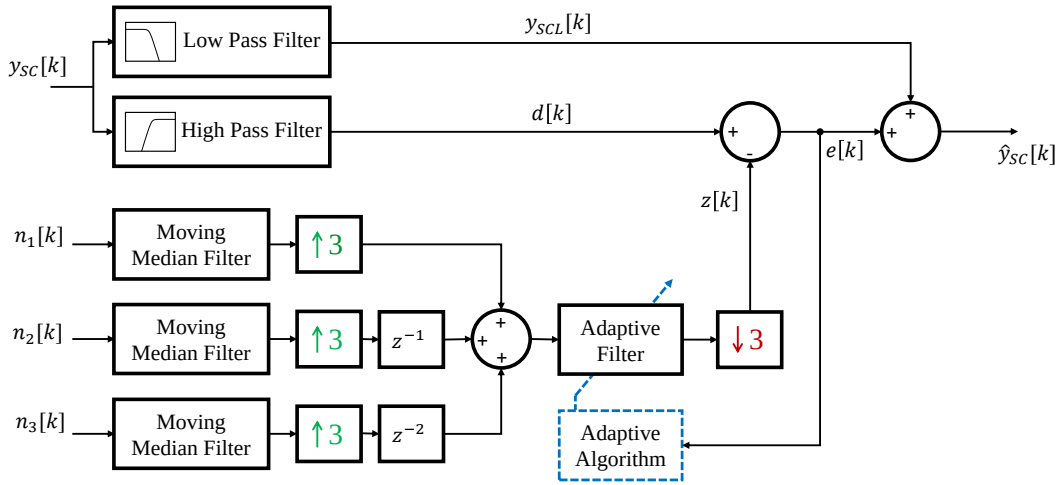

FIGURE 1: **An Overview of Motion Artifact Reduction Algorithm:** The above block diagram depicts multirate adaptive filtering architecture for motion artifact reduction from SC recording with three channel accelerometer recordings as the noise source reference. Figure shows how multi-channel noise reference stream is combined to a single stream via upsampling and delaying before feeding into adaptive filter. On the other hand SC is decomposed into $d[k]$ and $y_{SCL}[k]$ high pass and low pass filters respectively. The error between high frequency components $d[k]$ and adaptive filter artifact estimation $z[k]$ is denoted as $e[k]$ and is being fed back to the adaptive algorithm to update the adaptive filter coefficients.

three-dimensional linearized state-space model to describe the SC fluctuations from [46],

$$\dot{s}_1(t) = -\frac{1}{\tau_r}s_1(t) + u(t), \qquad \text{(sweat production)}$$
$$\dot{s}_2(t) = \frac{\eta s_1(t)}{\tau_r}s_1(t) - \frac{1}{\tau_p}s_2(t), \qquad \text{(pore collapse)}$$
$$\dot{s}_3(t) = \frac{(1-\eta)s_1(t)}{\tau_r}s_1(t) - \frac{1}{\tau_d}s_3(t) \qquad \text{(slow re-absorption)}$$

where $s_1(t)$, $s_2(t)$, and $s_3(t)$ states respectively represent the amount of sweat in the sweat ducts, the fraction of sweat in the ducts that are electrically conducted to the surface due to the open pore, and the fraction of sweat that is diffused in the corneum. The parameters τ_p and τ_d represent the faster decay time due to fast re-absorption and the slow decay time related to slow elimination (due to the cumulative effect of re-absorption, diffusion in the deeper corneum and evaporation), respectively. The parameter τ_r denotes the rise time of the SC. System input $u(t)$ represents the activation of ANS. To keep the definition simple, we assume that ANS activation occurs during the integer multiple of the sampling period. Let T_s be the sampling period. With the sparsity assumption as in [3], i.e. the number of activation events is very small compared to the number of samples in SC, we represent the activation of ANS as $u(t) = \sum_{k=1}^{K} u[k]\delta(t - kT_s)$ where $u[k]$ is the amplitude of the impulse during the activation of ANS at time kT_s; here, $u[k]$ is zero if there is no impulse in the stimuli. Here, we set the parameter $\eta = 0.5$ similarly to [46]. We represent the continuous state-space model as

$$\dot{s}(t) = A_c s(t) + B_c u(t),$$
$$y_{SC}(t) = C_c s(t) + \nu(t),$$

where, $s(t) = \begin{bmatrix} s_1(t) & s_2(t) & s_3(t) \end{bmatrix}^\top$,
$A_c = \begin{bmatrix} -\frac{1}{\tau_r} & 0 & 0 \\ +\frac{\eta_p}{\tau_r} & -\frac{1}{\tau_p} & 0 \\ +\frac{\eta_d}{\tau_r} & 0 & -\frac{1}{\tau_d} \end{bmatrix}$, $B_c = \begin{bmatrix} 1 \\ 0 \\ 0 \end{bmatrix}$,
$\boldsymbol{C}_c = \begin{bmatrix} 0 & 1 & 1 \end{bmatrix}$, The phasic and tonic components of SC can be represented as follows.

$$y_p(t) = C_{c,s}s(t) + \nu_s(t),$$
$$y_s(t) = C_{c,p}s(t) + \nu_p(t),$$

where, $\boldsymbol{C}_{c,p} = \begin{bmatrix} 0 & 1 & 0 \end{bmatrix}$, $\boldsymbol{C}_{c,s} = \begin{bmatrix} 0 & 0 & 1 \end{bmatrix}$. The discretized state-space model is as follows,

$$s[k] = A_d s[k-1] + B_d u[k], \tag{8}$$
$$y_S C[k] = C_d s[k] + \nu[k]. \tag{9}$$

where $s[k]$, $y[k] \in \mathbb{R}$, $u[k]$, $\nu[k]$ denote the state vector, observation, ANS activation, and measurement error in the discrete domain. The vector $\boldsymbol{u} = [u[1] \quad u[2] \quad \cdots \quad u[K]]^\top$ represents the ANS activation over the duration of the SC data. Here, $\boldsymbol{A}_d = e^{\boldsymbol{A}_c T_s}$, $\boldsymbol{B}_d = \int_0^{T_s} e^{\boldsymbol{A}_c(T_s-\rho)}B_c d\rho$, and $\boldsymbol{C}_d = \boldsymbol{C}_c$. We further define the tonic and phasic components. Here, T_s represents the sampling frequency. With this discrete state-space representation, we perform deconvolution using the scalable iterative reweighted Bayesian filtering-based *expectation-maximization* (EM) approach, called BayesianEDA [46], to identify $u[k]$, $\forall k \in \{1, 2, 3, \ldots, K\}$, i.e., the discretized version of $u(t)$ as well

as the physiological system parameters. The deconvolution is performed with a downsampled version of the noise-reduced signal with a sampling frequency of 4 Hz.

D. ISOLATING RESPIRATION-INDUCED SC ACTIVATION

Unlike the motion artifact in EDA, respiration-induced artifacts are more complex, i.e., mapping from deep breath respiration signal to the corresponding EDA response (which has a specific characteristic shape) is highly non-linear and not suitable to be modeled with adaptive filters. When someone takes a deep breath, there is a SC response that looks exactly the same as SC responses. However, if one knows at what time the deep breath happens, these responses can be easily isolated via deconvolution of SC data. More specifically, deep breath induces SC activation which can be isolated from the other SC activation. To isolate the respiration-induced activation of the SC, deep breaths must be detected, as mainly deep breaths are responsible for such SC responses. We consider two aspects of respiration for the detection of deep breaths. Firstly, deep breathing takes a bit longer. Second, deep breath generates higher stress on the respiration belt, i.e. the corresponding recorded voltage from the transducer will have a higher amplitude. We only considered respiration signals that are not motion-corrupted based on visual inspection.

First, we perform a continuous wavelet transform of the respiration signal. From all the wavelet coefficients, we keep those related to the $0.05 - 0.25$ Hz frequency components and perform an inverse wavelet transform to obtain the reconstructed respiration signal. One should note that the band pass filtering with FIR/IIR filter should also serve the purpose. In this way, we remove any potential high-frequency components related to normal breathing [49] and noise along with any potential DC component related to the baseline shift because of movement in the respiration belt. As the next step, we detect the breathing amplitude variation over time. Then we perform moving average filtering with a window size of 5 seconds on the absolute value of the respiration signal. Here, the window size is selected to be around the maximum length of a normal breath, which is about 5 seconds. We tried with different size of the window from 0 to 20 with 2 seconds increment, by visual inspection, a 5 seconds window seemed reasonable to us in terms of detecting high stress in the belt. The moving average of the absolute value of the respiration signal will be higher where the respiration belt stress is higher. We use the '*movmean*' function of MATLAB [50]. Then we obtain a moving standard deviation of the moving mean signal with a window of 30 seconds and take the sample-wise ratio of the moving mean signal and the moving standard deviation signal. This ratio standardizes the signal according to the 30-second window. Standardization accounts for different levels of fluctuations related to variable belt tightness levels. Variability in the belt tightness levels of the transducer belt may originate from changes in the participant's pose or changes in the belt position during the experiment. Next, we subtract the mean from the ratio signal and multiply it by 3. Finally, we perform a sigmoid transformation to map the signal between 0 and 1 to represent the probability. We define this probability as $p_1[k]$.

Second, we perform peak detection on the wavelet-reconstructed respiration signal and peak detection on the negative of it. For peak detection, we use '*findpeaks*' from MATLAB with default settings [50]. We take both amplitude and locations of the peaks from the reconstructed and negative reconstructed signals to perform a spline interpolation. Then we obtained a moving standard deviation of the interpolated signal with a window of 90 seconds. Finally, we take the sample-wise ratio of the interpolated signal and the moving standard deviation signal. This ratio standardizes the signal based on the 90-second window and accounts for high levels of fluctuations with different tightness levels of the transducer belt because of changes in the participant's pose. Finally, we multiply the ratio signal by 10 and perform a sigmoid transformation to map the signal between 0 to 1 to represent probability. We define this probability as $p_2[k]$. We multiply these two probabilities to obtain one probability signal representing the probability of a deep breath. Let us denote this probability by $p[k]$. Therefore, we can write $p[k] = p_1[k]p_2[k]$. We obtain the probability with 100 Hz sampling frequency and then down-sample in order to match the deconvolution results.

After deconvolution with the BayesianEDA algorithm to obtain ANS activation, we define respiration-induced activation as $u[k]p[k]$ and direct activation of ANS as $u[k](1-p[k])$. Here, the deconvolution with BayesianEDA algorithm is performed at 4 Hz. Therefore, $p[k]$ was downsampled at the same sampling frequency to obtain $u[k]p[k]$ and $u[k](1 - p[k])$.

E. INVESTIGATE ADAPTIVE FILTERS WITH KNOWN SIMULATED NOISE

The objective of the simulated study is to have an idea of the performance of four different adaptive filters in the removal of artifacts from SC data. For the simulated study, we first generate a reference noise signal and then perform a non-linear transformation to add it to the raw signals from the publicly available dataset in [47]. The noise reference is generated by summation of a sine wave and a square wave where the amplitude and the frequencies are randomly varied. Square wave-type artifacts are representation of sensor saturation effect. On the other hand, sign wave is representative of rhythmic motions due to movements such as running or jogging. The reason of using these two types of signal along with Gaussian noise is the effort towards motion artifacts closer to reality. For the simulation purpose, we vary the amplitude of the waves that are sampled from a Gaussian distribution every second with the mean of 20% of the standard deviation of the corresponding SC recording. On the other hand, the standard deviation of the random amplitude has been selected to be 5% of the standard deviation of the corresponding SC recording amplitudes. Similarly, for the frequencies, we sampled every 0.5 seconds randomly from a

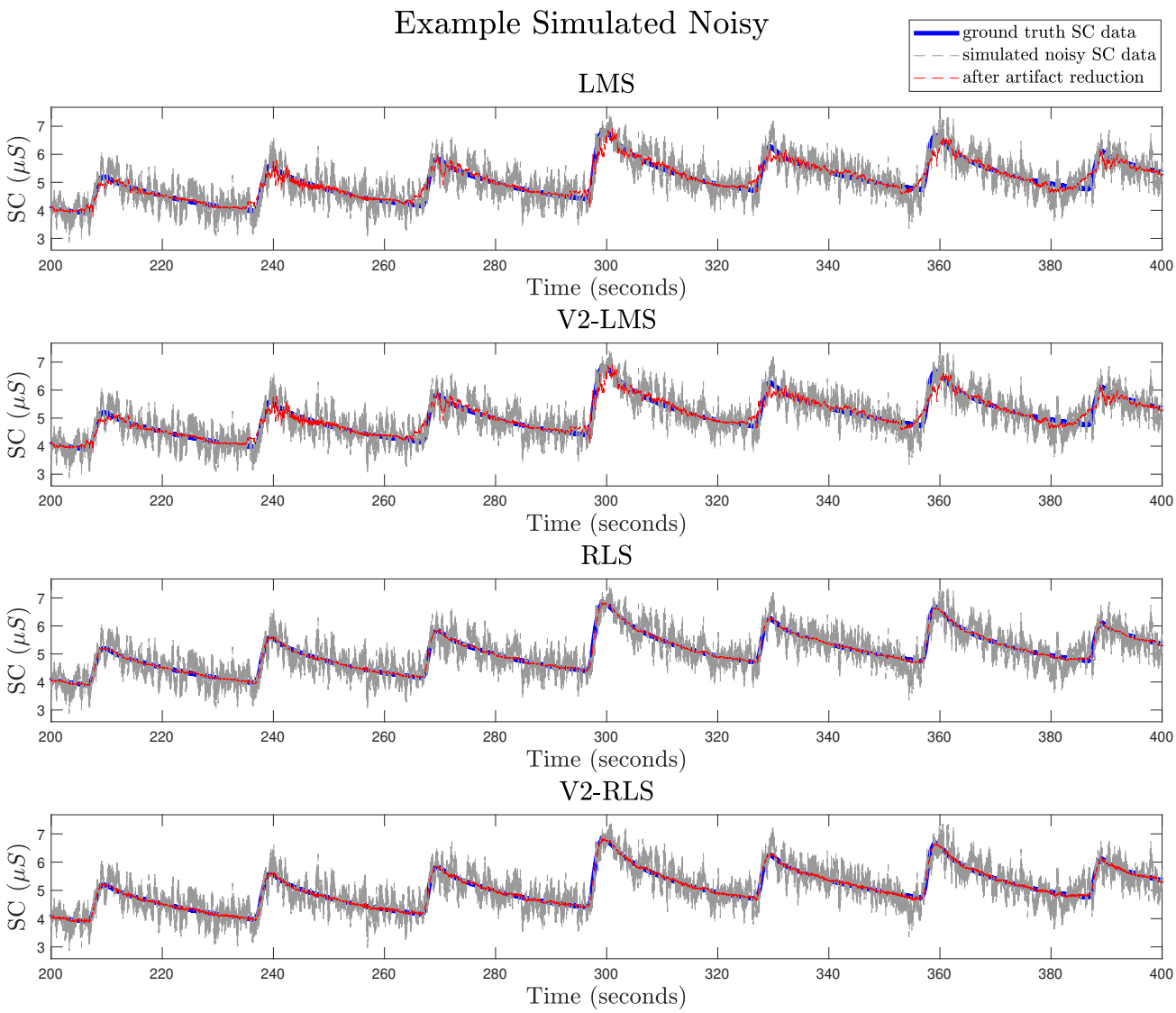

FIGURE 2: **Non-linear Artifact Reduction Result Example with Simulated Noise Source.** Subplots from top to bottom show the artifact removal performance with LMS filter, V2-LMS, RLS, V2-RLS filter with a single noise reference.

Gaussian distribution of mean 1 Hz and variance 0.25 Hz. We also add zero mean Gaussian noise with a standard deviation of 0.2. The sampling frequency for discretization is selected as 100 Hz, which is the same as the sampling frequency of the dataset. We utilize the following transformation for simulating the artifact-corrupted SC signal as follows,

$$y_{SC}[k] = y^{D}_{SC}[k] + (h * n)[k] + c_1(n[k])^2 + c_2(n[k])^3. \tag{10}$$

where h is a filter representing the transformation of the noise. We generate it first by drawing 50 samples from zero-mean Gaussian distributed number to create a vector h_r then scale it by dividing it by its norm to find the filter, i.e., $h = \frac{h_r}{||h_r||_2}$. Furthermore, c_1 and c_2 are randomly sampled from Gaussian distributed random variables with a standard deviation of 0.1 and 0.01. Here, y^{D}_{SC} represents the SC signals from the publicly available datasets. k denotes the k^{th} sample. We successfully utilized the artifact removal with the adaptive filter with parameters $\alpha = 0.02$ and $\lambda = 0.999995$. These values were selected by trial and error and visual inspection of the results for all the data corresponding to 26 participants in [47].

II. RESULTS

A. SIMULATION RESULTS

Figure 2 shows the results of the LMS, V2-LMS, RLS, and V2-RLS filtering. The visual depiction shows that the adaptive filters can remove most of the simulated noise. The

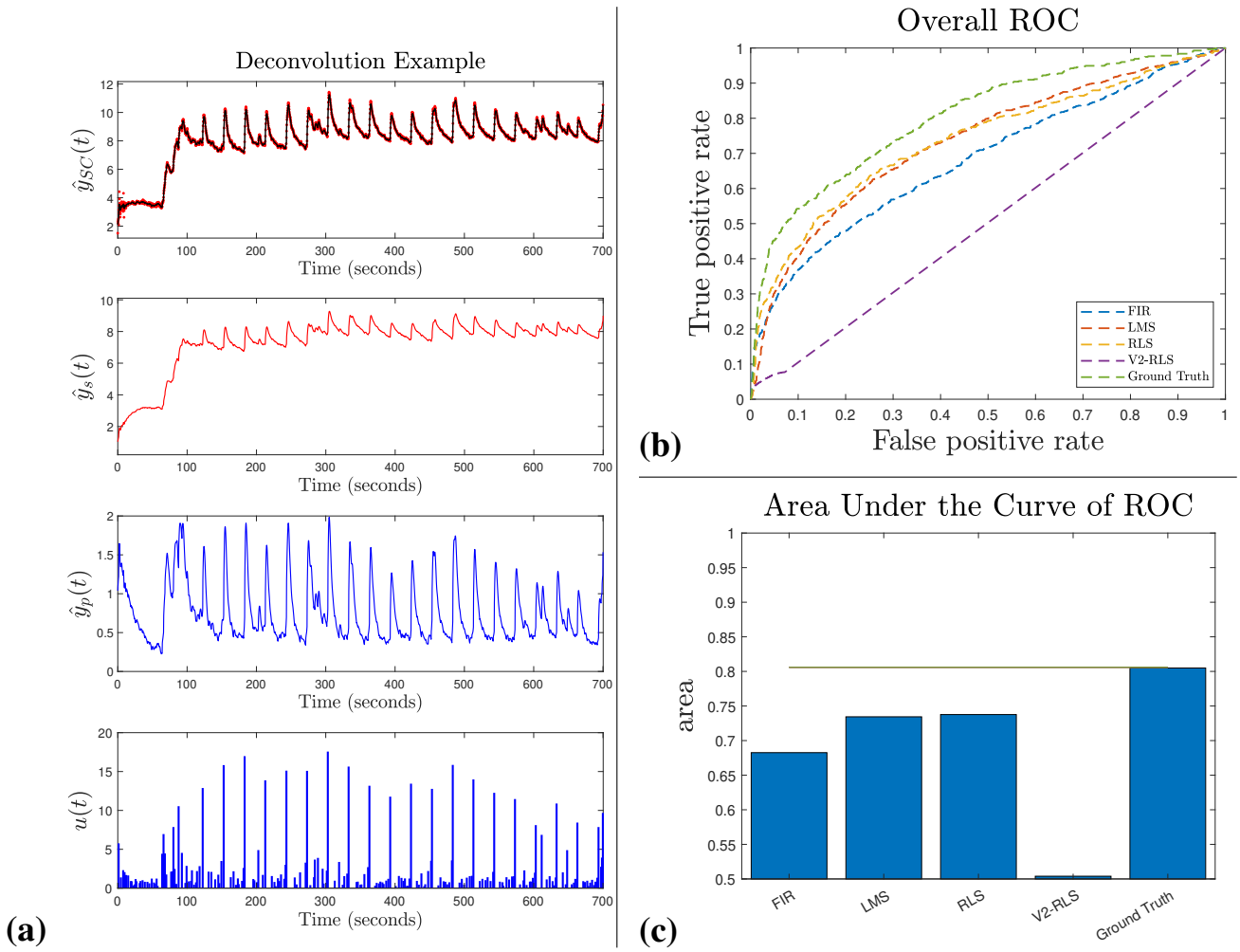

FIGURE 3: **Inference Performance of ANS Activation After Deconvolution Algorithm After Artifact Removal with Different Filters**. (a) Example of deconvolution (top to bottom sub-plots depict raw signals in red with reconstructed signal in black, tonic component, phasic component and identified ANS activations, respectively), (b) receiver operating characteristic (ROC) curves of detection performance of event related SC responses after reducing artifacts with different approaches, and (c) area under the curves (AUC) for ROCs.

result also shows a qualitative illustration that RLS and V2-RLS are performing better in terms of their ability to follow the ground truth. Moreover, results from RLS and V2-RLS filters were always stable while LMS and V2-LMS filters became unstable for 5 participants and could not be used for further analysis.

Using stable adaptive filtering results, we deconvolve the artifact-reduced SC signal to perform deconvolution with BayesianEDA algorithm [46]. Figure 3-(a) shows an example deconvolution result showing the inferred activation of ANS from the artifact-reduced signal. Furthermore, we use the estimated activation of ANS $u(t)$ to distinguish between event-related SCRs and non-event-related SCRs. Here, the events are loud sound events. First, we label all nonzero elements in estimated $u[k]\ \forall k$ as positive if they are within 5 seconds after the participant heard a loud sound event, and other impulses as negative. We consider the values of non-zero elements to be the only feature for the classification within the participants to investigate the receiver operating characteristic (ROC) [51], [52]. Figure 3-(b) shows the ROCs obtained from the filtered signal from the FIR lowpass filter with 0.5 Hz cutoff, LMS adaptive filter, RLS adaptive filter, and V2-RLS adaptive filter. Figure 3-(c) shows the corresponding area under the curve (AUC) of the ROCs. The results show that the RLS-filtered signals yield the highest AUC (≈ 0.738).

B. EXPERIMENTAL RESULTS

We applied all four types of adaptive filters on the experimental data with different settings; however, only the RLS filter provided stable results while learning. Therefore, we present only results from the RLS filter for the experimental study.

The SC and three-axis accelerometer signals are resampled to 100 Hz. Based on the adaptive filtering scheme in Figure 1, the desired signal has a sampling frequency of 100 Hz, and the noise reference has a sampling frequency of 300 Hz. The adaptive filter length is also $L = 300$ to consider a 1 second window. For the forgetting factor, we first tested the value that has been used for the simulated data. Based on the results, we relaxed the forgetting factor to allow the filter to re-adjust itself for newer data well. Through trial and error, $\lambda = 0.999$ seemed to work well for our study. Figure 4 shows an example adaptive filtering result utilizing the RLS adaptive filter. Figure 4 also shows that some of the peaks that are seen in the captured motion information power spectrum density of the accelerometer are also can be seen in the raw experimental power spectrum density of the SC signal. RLS adaptive filter could successfully remove those peaks. Figure 4, also depicts that there is a significant amount of energy reduction in the power spectrum density. Additional results for all participants are provided in the Appendix. Figure 5 shows some zoomed-in segments from all trials of Participants 1 and 2. The figure provides a qualitative illustration of RLS adaptive filters' ability to reduce artifacts utilizing accelerometer information.

Additionally, we try to identify SCR activation related to the deep breaths. We only utilize the respiration signal for Trial 1-5 for Participant 1. Because other respiration signals seemed to be heavily corrupted with artifacts reducing artifacts in respiration signals is out of the scope of this study. First, we successfully detected deep respirations based on the method described in Section I-D. Figure 6 represents the results of the deep breath detection. Next, we deconvolve the motion artifact-reduced SC signals and identify the respiration-induced SC activation based on the estimated probability $p[k]$. Figure 7 shows the results of the identification of respiration-induced activation for SCR generation.

III. DISCUSSION

In this study, we first investigated four different adaptive filter candidates with simulated data and evaluated their performance based on the identification of ANS performance from the artifact-reduced signals. Then we perform experiments to collect motion artifact corrupted SC data along with motion reference signal (accelerometer sensor data and respiration signal). Then we evaluate performance artifact removal performance of the linear-RLS filter from experimental data. Finally, we propose a method for identifying and separating respiration-induced artifacts from ANS activation utilizing Bayesian filter-based deconvolution algorithm. From the simulated study with publicly available experimental SC data [47], we can see that the RLS filter performs better than other filters in terms of retaining information about event-related responses so that detection of such events is detected. Moreover, the linear RLS filter is the most stable one. Although we have considered some nonlinearity in the noise reference transformation, the RLS filter was able to model the transformation with a time-varying piecewise linear fashion. However, LMS, V2-LMS and V2-LMS filters suffer from instability and the high number of parameters required to update each step compared to the number of observations used during gradient calculation. Further analysis with deconvolution on artifact-reduced SC data and consequent loud-sound detection confirms that the RLS filter is reasonably improving the detection ability of event-related activations for SCR generation.

From the analysis of our experimental study, we see that only the RLS filter was able to achieve stability in terms of reducing the motion artifact. However, none of the other filters was able to achieve stable results. The power spectrum density change also confirms that there is a significant reduction in the spectrum peaks that are generated by motion. We observe some peaks in the accelerometer power spectrum. The similarities are also seen in the power spectrum of raw SC data denoting the artifacts. After artifact removal, these spectrum peaks are not visible anymore. In Figure 5, we also see that how different types of artifacts are reduced. In some cases, we have seen that the RLS filter output becomes more noisy than the input. These scenarios suggest significant changes in the transformation system between the accelerometer data to artifact generation. The RLS filter takes some time to learn the new system and inaccuracy in the reduction can be seen during this learning phase.

Furthermore, we see that a simple rule-based algorithm combined with BayesianEDA [46] can lead to the successful identification of the deep-breath and deep-breath-induced SCR responses. In this way, direct ANS activation can be isolated from respiration-induced activation. Thus, the respiration-induced alteration of SC data can be ignored in some applications of autonomic arousal estimation by modifying the state-space formulations in [5], [14], [15], [53]. However, we have considered some intuitive rule-based algorithm for deep breath detection.

For this study, we have generated simulated noise with some arbitrary settings. Therefore, it might not be capturing the whole space of artifact corruption. However, it allows us to obtain an idea of how different adaptive filters might perform in real-world settings. For the experimental data, we have suggested the participants look the screen and try to generate artifacts by hand waving and in-place jogging with multiple trials which might be slightly different than the reality. However, this experimental dataset is a stepping stone to evaluate motion artifact-contaminated data and corresponding artifact reduction algorithms. In the future, we plan to perform more experiments with different scenarios and different activities such that the dataset approximately represents the real-world motion artifact space. For this investigation, the experimental part has been beneficial to evaluate adaptive filters in a qualitative manner. One possible future experiment can be performing physical activities during a loud sound event experiment [47]. Another future direction is to perform experiments by placing sensors and noise references from different skin locations such as the wrist.

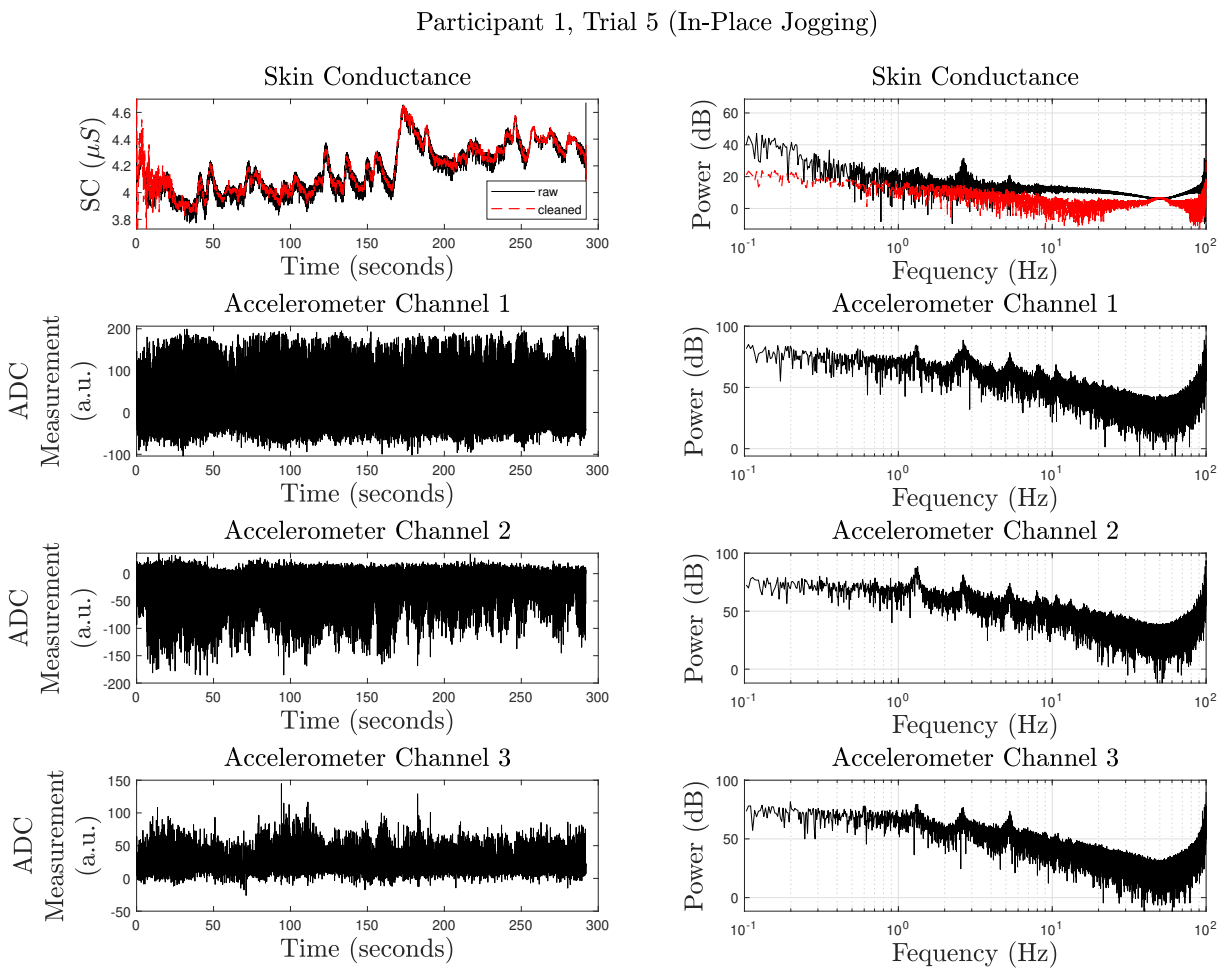

FIGURE 4: **Example Artifact Reduction Result with Multi-resolution RLS Adaptive Filter with Experimental SC recording From Participant 1, Trial 5, During In-Place Jogging.** The first left panel depicts raw (artifact corrupted) and cleaned (artifact reduced) SC data. The first right panel shows the corresponding power spectrum density. The next three panels show three accelerometer channel recordings on the left and their corresponding power spectrum density on the right.

As mentioned in both the experimental and simulated study results, there have been many cases of unstable results. RLS filter seemed to be more stable for the selected value for both the simulated and the experimental data. LMS and V2-LMS have shown instability for some examples of simulated data (5 out of 26 participants) and have always been unstable for the experimental dataset. V2-RLS also showed unstable results only for the experimental dataset. For unstable results, the coefficients of the adaptive filter values explode to infinity. To handle stability, we plan to utilize techniques such as regularization in the cost function similar to [54]. Another possible future direction to handle instability is to use techniques such as leaky LMS/RLS algorithms [55], [56].

We have only utilized accelerometer data for the noise reference. We observe that the accelerometer data-based noise is noise reference is helping to reduce a significant amount of artifacts. However, we only placed an accelerometer on one of the electrodes while the motion artifact could be a resultant of motion on both the electrodes on both hands. Therefore, an additional accelerometer sensor on the other electrode can potentially improve the results. Moreover, accelerometers are not good at capturing some types of motion information. For example, if someone bends their finger resulting in some pressure on the electrodes will lead to a magnitude artifact that might not be captured in the accelerometer reading. Moreover, the orientation of the hand might also lead to a change in the sensor placement. Therefore, more noise reference sensors such as gyroscopes, magnetometers, and pressure sensors should be investigated in a systematic manner.

From results we can see that RLS filter is reasonably performing in terms of reducing motion artifact. As RLS filters are updated at each time step, the resulting filters act as a piecewise linear transformation of the noise reference $x[k]$ such that the error signal $e[k]$ is minimized. Thus, the non-linearity that has been introduced by the RLS filter might not be enough. On the other hand, the volterra-series-based nonlinearity requires huge number of coefficients, which

might lead to over-fitting and instability. One potential future direction of this study is to investigate neural networks [57] or adaptive filters based on functional links [58] to better realize the nonlinear transformation with a lower number of coefficients.

Finally, to assess the effectiveness of the proposed denoising approach, a quantitative evaluation of the noise removal effect is needed where a noiseless ground-truth reference is a must. However, with the current experimental setup obtaining ground truth SC data as well as motion artifact contamination is impossible. The only way to achieve this is to provide a known emotional stimulus such as a loud sound and see how well the SC response due to the stimulus is detected after and before motion artifact removal, similar to our simulated study. Therefore, we plan to experiment in the future similar to a loud sound experiment, in the presence of a motion artifact.

IV. CONCLUSION

In this study, we have investigated linear and nonlinear adaptive filters in terms of artifact reduction performance. We have utilized BayesianEDA algorithm to deconvolve the SC data to identify the activations. We utilized simulated data utilizing publicly available datasets as well as the experimental study in order to quantitatively and qualitatively investigate different filters. Our investigation shows that RLS filter performed best based on our experimental dataset. We further show that deep breath detection and BayesianEDA algorithm can be utilized to identify the deep breath-induced activations and corresponding SCRs. In this study, to show the feasibility of reducing respiration-induced artifacts in SCR, we collected a small experimental dataset and developed the proposed algorithm as a first step for moving toward the real-world use of SCR in tracking cognitive arousal and mental well-being. In the future, we plan to develop an improved deep breath detection algorithm (specifically, those responsible for the SCR generation in SC data) by collecting a large dataset and utilizing a data-driven machine learning approach. In conclusion, this study is an important step towards the implementation of SC signal-based ANS activation detection [11]–[13], [46], arousal estimation [5], [14], [15], [53], and the corresponding control design for an effective mobile brain-machine interface architecture for emotional stress management [16], [59]–[61].

.

APPENDIX A ADDITIONAL RESULTS

Additional figures showing the motion artifact removal performance for all the experimental data collected from two participants.

REFERENCES

[1] M. R. Amin and R. T. Faghih, "Identification of sympathetic nervous system activation from skin conductance: A sparse decomposition approach with physiological priors," IEEE Transactions on Biomedical Engineering, vol. 68, no. 5, pp. 1726–1736, 2020.

[2] W. Boucsein, Electrodermal activity. Springer Science & Business Media, 2012.

[3] R. T. Faghih, P. A. Stokes, M.-F. Marin, R. G. Zsido, S. Zorowitz, B. L. Rosenbaum, H. Song, M. R. Milad, D. D. Dougherty, and E. N. Eskandar, "Characterization of fear conditioning and fear extinction by analysis of electrodermal activity," in Engineering in Medicine and Biology Society (EMBC), 2015 37th Annual International Conference of the IEEE, 2015, pp. 7814–7818.

[4] D. R. Bach, G. Flandin, K. J. Friston, and R. J. Dolan, "Modelling event-related skin conductance responses," International Journal of Psychophysiology, vol. 75, no. 3, pp. 349–356, 2010.

[5] D. S. Wickramasuriya, C. Qi, and R. T. Faghih, "A state-space approach for detecting stress from electrodermal activity." in Annual International Conference of the IEEE Engineering in Medicine and Biology Society. IEEE Engineering in Medicine and Biology Society. Annual Conference, vol. 2018, 2018, pp. 3562–3567.

[6] A. Y. Kim, E. H. Jang, S. Kim, K. W. Choi, H. J. Jeon, H. Y. Yu, and S. Byun, "Automatic detection of major depressive disorder using electrodermal activity," Scientific reports, vol. 8, no. 1, pp. 1–9, 2018.

[7] Y. Kong, H. F. Posada-Quintero, and K. H. Chon, "Pain detection using a smartphone in real time," in 2020 42nd Annual International Conference of the IEEE Engineering in Medicine & Biology Society (EMBC). IEEE, 2020, pp. 4526–4529.

[8] H. F. Posada-Quintero, J. B. Bolkhovsky, M. Qin, and K. H. Chon, "Human performance deterioration due to prolonged wakefulness can be accurately detected using time-varying spectral analysis of electrodermal activity," Human factors, vol. 60, no. 7, pp. 1035–1047, 2018.

[9] M. Sarchiapone, C. Gramaglia, M. Iosue, V. Carli, L. Mandelli, A. Serretti, D. Marangon, and P. Zeppegno, "The association between electrodermal activity (eda), depression and suicidal behaviour: A systematic review and narrative synthesis," BMC psychiatry, vol. 18, no. 1, pp. 1–27, 2018.

[10] H. F. Azgomi, I. Cajigas, and R. T. Faghih, "Closed-loop cognitive stress regulation using fuzzy control in wearable-machine interface architectures," IEEE Access, vol. 9, pp. 106 202–106 219, 2021.

[11] M. R. Amin and R. T. Faghih, "Inferring autonomic nervous system stimulation from hand and foot skin conductance measurements," in 2018 52nd Asilomar Conference on Signals, Systems, and Computers. IEEE, 2018, pp. 655–660.

[12] ——, "Sparse deconvolution of electrodermal activity via continuous-time system identification," IEEE Transactions on Biomedical Engineering, 2019.

[13] ——, "Robust inference of autonomic nervous system activation using skin conductance measurements: A multi-channel sparse system identification approach," IEEE Access, vol. 7, pp. 173 419–173 437, 2019.

[14] D. S. Wickramasuriya and R. T. Faghih, "A bayesian filtering approach for tracking arousal from binary and continuous skin conductance features," IEEE Transactions on Biomedical Engineering, 2019.

[15] D. S. Wickramasuriya, M. Amin, R. T. Faghih et al., "Skin conductance as a viable alternative for closing the deep brain stimulation loop in neuropsychiatric disorders," Frontiers in neuroscience, vol. 13, p. 780, 2019.

[16] H. F. Azgomi, D. S. Wickramasuriya, and R. T. Faghih, "State-space modeling and fuzzy feedback control of cognitive stress," in 2019 41st Annual International Conference of the IEEE Engineering in Medicine and Biology Society (EMBC). IEEE, 2019, pp. 6327–6330.

[17] Y.-L. Zheng, X.-R. Ding, C. C. Y. Poon, B. P. L. Lo, H. Zhang, X.-L. Zhou, G.-Z. Yang, N. Zhao, and Y.-T. Zhang, "Unobtrusive sensing and wearable devices for health informatics," IEEE Transactions on Biomedical Engineering, vol. 61, no. 5, pp. 1538–1554, 2014.

[18] Y. Guo, X. Liu, S. Peng, X. Jiang, K. Xu, C. Chen, Z. Wang, C. Dai, and W. Chen, "A review of wearable and unobtrusive sensing technologies for chronic disease management," Computers in Biology and Medicine, p. 104163, 2020.

[19] G. Aroganam, N. Manivannan, and D. Harrison, "Review on wearable technology sensors used in consumer sport applications," Sensors, vol. 19, no. 9, p. 1983, 2019.

[20] D. Biswas, N. Simões-Capela, C. Van Hoof, and N. Van Helleputte, "Heart rate estimation from wrist-worn photoplethysmography: A review," IEEE Sensors Journal, vol. 19, no. 16, pp. 6560–6570, 2019.

[21] T. Pereira, N. Tran, K. Gadhoumi, M. M. Pelter, D. H. Do, R. J. Lee, R. Colorado, K. Meisel, and X. Hu, "Photoplethysmography based atrial fibrillation detection: a review," NPJ digital medicine, vol. 3, no. 1, pp. 1–12, 2020.

[22] L.-M. Bai, M.-H. Fan, C.-H. Feng, and L.-H. Wang, "Using an adaptive filter to remove ecg motion artifact interference," in 2018 IEEE International Conference on Consumer Electronics-Taiwan (ICCE-TW). IEEE, 2018, pp. 1–2.

[23] W. Dargie and J. Lilienthal, "Review of motion artifacts removing techniques for wireless electrocardiograms," in 2020 IEEE 23rd International Conference on Information Fusion (FUSION). IEEE, 2020, pp. 1–8.

[24] A. Kilicarslan and J. L. C. Vidal, "Characterization and real-time removal of motion artifacts from eeg signals," Journal of neural engineering, vol. 16, no. 5, p. 056027, 2019.

[25] P. S. Diniz et al., Adaptive filtering. Springer, 1997, vol. 4.

[26] Y. Ye, Y. Cheng, W. He, M. Hou, and Z. Zhang, "Combining nonlinear adaptive filtering and signal decomposition for motion artifact removal in wearable photoplethysmography," IEEE Sensors Journal, vol. 16, no. 19, pp. 7133–7141, 2016.

[27] S. S. Chowdhury, R. Hyder, M. S. B. Hafiz, and M. A. Haque, "Real-time robust heart rate estimation from wrist-type ppg signals using multiple reference adaptive noise cancellation," IEEE journal of biomedical and health informatics, vol. 22, no. 2, pp. 450–459, 2016.

[28] C. S. Kim, J. Sun, D. Liu, Q. Wang, and S. G. Paek, "Removal of ocular artifacts using ica and adaptive filter for motor imagery-based bci," IEEE/CAA journal of automatica sinica, 2017.

[29] C. Beach, M. Li, E. Balaban, and A. J. Casson, "Motion artefact removal in electroencephalography and electrocardiography by using multichannel inertial measurement units and adaptive filtering," Healthcare Technology Letters, vol. 8, no. 5, p. 128, 2021.

[30] C.-K. Kim, S. Lee, D. Koh, and B.-M. Kim, "Development of wireless nirs system with dynamic removal of motion artifacts," Biomedical Engineering Letters, vol. 1, no. 4, pp. 254–259, 2011.

[31] S. Yadav, S. K. Saha, R. Kar, and D. Mandal, "Eeg/erp signal enhancement through an optimally tuned adaptive filter based on marine predators algorithm," Biomedical Signal Processing and Control, vol. 73, p. 103427, 2022.

[32] L. A. M. Jefri, F. A. Rahman, N. A. Malik, and F. N. M. Isa, "Eye blink identification and removal from single-channel eeg using emd with energy threshold and adaptive filter," IIUM Engineering Journal, vol. 24, no. 2, pp. 141–158, 2023.

[33] P. Sharma, "Removal of artifacts in eeg signals using sign based lms adaptive filtering techniques," in 2023 1st International Conference on Innovations in High Speed Communication and Signal Processing (IHCSP). IEEE, 2023, pp. 199–203.

[34] C. Wan, D. Chen, and J. Yang, "Pulse rate estimation from forehead photoplethysmograph signal using rls adaptive filtering with dynamical reference signal," Biomedical Signal Processing and Control, vol. 71, p. 103189, 2022.

[35] R. Nagal, P. Kumar, and P. Bansal, "Optimization of adaptive noise canceller with grey wolf optimizer for eeg/erp signal noise cancellation," in 2019 6th International Conference on Signal Processing and Integrated Networks (SPIN). IEEE, 2019, pp. 670–675.

[36] S. Gupta, A. K. Sahoo, and U. K. Sahoo, "Volterra and wiener model based temporally and spatio-temporally coupled nonlinear system identification: a synthesized review," IETE Technical Review, vol. 38, no. 3, pp. 303–327, 2021.

[37] K. T. Johnson and R. W. Picard, "Advancing neuroscience through wearable devices," Neuron, vol. 108, no. 1, pp. 8–12, 2020.

[38] S. Taylor, N. Jaques, W. Chen, S. Fedor, A. Sano, and R. Picard, "Automatic identification of artifacts in electrodermal activity data," in 2015 37th Annual International Conference of the IEEE Engineering in Medicine and Biology Society (EMBC). IEEE, 2015, pp. 1934–1937.

[39] Y. Zhang, M. Haghdan, and K. S. Xu, "Unsupervised motion artifact detection in wrist-measured electrodermal activity data," in Proceedings of the 2017 ACM International Symposium on Wearable Computers, 2017, pp. 54–57.

[40] S. Subramanian, B. Tseng, R. Barbieri, and E. N. Brown, "An unsupervised automated paradigm for artifact removal from electrodermal activity in an uncontrolled clinical setting," Physiological Measurement, 2022.

[41] J. Llanes-Jurado, L. A. Carrasco-Ribelles, M. Alcañiz, and J. Marín-Morales, "Automatic artifact recognition and correction for electrodermal activity in uncontrolled environments," 2021.

[42] M. B. Hossain, H. Posada-Quintero, and K. Chon, "A deep convolutional autoencoder for automatic motion artifact removal in electrodermal activity," IEEE Transactions on Biomedical Engineering, 2022.

[43] W. Chen, N. Jaques, S. Taylor, A. Sano, S. Fedor, and R. W. Picard, "Wavelet-based motion artifact removal for electrodermal activity," in 2015 37th Annual International Conference of the IEEE Engineering in Medicine and Biology Society (EMBC). IEEE, 2015, pp. 6223–6226.

[44] R. Schneider, S. Schmidt, M. Binder, F. Schäfer, and H. Walach, "Respiration-related artifacts in eda recordings: introducing a standardized method to overcome multiple interpretations," Psychological reports, vol. 93, no. 3, pp. 907–920, 2003.

[45] G. Lee, B. Choi, H. Jebelli, C. R. Ahn, and S. Lee, "Reference signal-based method to remove respiration noise in electrodermal activity (eda) collected from the field," in Computing in civil engineering 2019: Data, sensing, and analytics. American Society of Civil Engineers Reston, VA, 2019, pp. 17–25.

[46] R. Amin and R. T. Faghih, "Physiological characterization of electrodermal activity enables scalable near real-time autonomic nervous system activation inference," PLOS Computational Biology, vol. 18, no. 7, p. e1010275, 2022.

[47] D. R. Bach, G. Flandin, K. J. Friston, and R. J. Dolan, "PsPM-SCRV10: Skin conductance responses to loud sounds, simultanously recorded from palm, fingers and foot," Feb. 2017. [Online]. Available: https://doi.org/10.5281/zenodo.291465

[48] L. Nyhof, I. Hettiarachchi, S. Mohammed, and S. Nahavandi, "Adaptive-multi-reference least means squares filter," in Neural Information Processing: 21st International Conference, ICONIP 2014, Kuching, Malaysia, November 3-6, 2014. Proceedings, Part III 21. Springer, 2014, pp. 527–534.

[49] M. A. Russo, D. M. Santarelli, and D. O'Rourke, "The physiological effects of slow breathing in the healthy human," Breathe, vol. 13, no. 4, pp. 298–309, 2017.

[50] MATLAB version 9.9.0.1467703 (R2020b), The Mathworks, Inc., Natick, Massachusetts, 2020.

[51] N. A. Macmillan and C. D. Creelman, Detection theory: A user's guide. Psychology press, 2004.

[52] C. S. Moskowitz and M. S. Pepe, "Quantifying and comparing the predictive accuracy of continuous prognostic factors for binary outcomes," Biostatistics, vol. 5, no. 1, pp. 113–127, 2004.

[53] D. S. Wickramasuriya and R. T. Faghih, "A marked point process filtering approach for tracking sympathetic arousal from skin conductance," IEEE Access, 2020.

[54] J. Benesty, C. Paleologu, and S. Ciochina, "On regularization in adaptive filtering," IEEE Transactions on Audio, Speech, and Language Processing, vol. 19, no. 6, pp. 1734–1742, 2010.

[55] K. A. Mayyas and T. Aboulnasr, "Leaky lms: A detailed analysis," in Proceedings of ISCAS'95-International Symposium on Circuits and Systems, vol. 2. IEEE, 1995, pp. 1255–1258.

[56] E. Horita, K. Sumiya, H. Urakami, and S. Mitsuishi, "A leaky rls algorithm: Its optimality and implementation," IEEE transactions on signal processing, vol. 52, no. 10, pp. 2924–2936, 2004.

[57] S. Selvan and R. Srinivasan, "Removal of ocular artifacts from eeg using an efficient neural network based adaptive filtering technique," IEEE Signal Processing Letters, vol. 6, no. 12, pp. 330–332, 1999.

[58] D. Comminiello, M. Scarpiniti, L. A. Azpicueta-Ruiz, J. Arenas-García, and A. Uncini, "Functional link adaptive filters for nonlinear acoustic echo cancellation," IEEE Transactions on Audio, Speech, and Language Processing, vol. 21, no. 7, pp. 1502–1512, 2013.

[59] H. F. Azgomi and R. T. Faghih, "A wearable brain machine interface architecture for regulation of energy in hypercortisolism," in 2019 53rd Asilomar Conference on Signals, Systems, and Computers. IEEE, 2019, pp. 254–258.

[60] L. R. Branco, A. Ehteshami, H. F. Azgomi, and R. T. Faghih, "Closed-loop tracking and regulation of emotional valence state from facial electromyogram measurements," Frontiers in computational neuroscience, vol. 16, p. 747735, 2022.

[61] H. F. Azgomi and R. T. Faghih, "Enhancement of closed-loop cognitive stress regulation using supervised control architectures," IEEE open journal of engineering in medicine and biology, vol. 3, pp. 7–17, 2022.

MD. RAFIUL AMIN (S'15-M'22) received his B.S. degree in electrical and electronic engineering from the Bangladesh University of Engineering and Technology, Dhaka, Bangladesh in 2016. He received his Ph.D. degree in Electrical and Computer Engineering at the University of Houston, Houston, TX, USA in 2021. He worked as a software engineer at Samsung R&D Institute Bangladesh Limited from 2016 to 2017. He currently serves as a DSP Characterization Engineer at Aeva, Inc., Mountain View, CA, USA, a position he assumed in January 2022.

SAMIUL ALAM received his B.S. degree in Electrical and Electronics Engineering from the Bangladesh University of Engineering and Technology, Dhaka, Bangladesh, and his M.S. degree in Computer Science from Michigan State University, East Lansing, MI, USA, in 2018 and 2023, respectively. He is currently pursuing a Ph.D. degree in Computer Science at Ohio State University, Columbus, OH, USA.

SAMAN KHAZAEI (S'21) received his B.S. degree in mechanical engineering from the Sharif University of Technology, Tehran, Iran, and his M.S. degree in electrical engineering from the University of Houston, Houston, TX, USA, in 2019 and 2021, respectively. He is pursuing a Ph.D. degree in biomedical engineering with the New York University, New York, NY, USA. He worked as a Renewable Energy Engineer at NOV Inc (National Oilwell Varco) from 2020 to 2021.

HAMID FEKRI AZGOMI obtained his PhD in electrical engineering with a specialized focus on closed-loop brain state regulation from the University of Houston, Texas, USA, in 2021. He had previously earned his M.S. and B.S. degrees in electrical engineering, with a concentration in control systems, in 2013 and 2010, respectively. During his doctoral studies, he conducted analyses of physiological signals collected via wearable devices to deduce internal brain states. His research also entailed the development of intricate control algorithms for the purpose of regulating brain states and closing the loop. Additionally, he conceptualized and executed human-subject experiments to explore the effects of utilizing safe actuation in the regulation of brain states and closing the loop. He is currently a postdoctoral scholar at the department of neurological surgery at University of California San Francisco (UCSF). In his current role at UCSF, he applies his background in control systems and signal processing to enhance existing adaptive deep brain stimulation practices for patients with Parkinson's disease.

ROSE T. FAGHIH (S'12-M'15-SM'2021) received her B.S. degree (summa cum laude) in electrical engineering (Hons.) from the University of Maryland, College Park, MD, USA, in 2008, and the S.M. and Ph.D. degrees in electrical engineering and computer science with a minor in mathematics from the Massachusetts Institute of Technology (MIT), Cambridge, MA, USA, in 2010 and 2014, respectively.

Dr. Faghih is an associate professor of Biomedical Engineering at the New York University (NYU) where she directs the Computational Medicine Laboratory within the NYU Langone Health's Tech4Health Institute. She completed her postdoctoral training at the Department of Brain and Cognitive Sciences and the Picower Institute for Learning and Memory at MIT as well as the Department of Anesthesia, Critical Care and Pain Medicine at Massachusetts General Hospital. At MIT, she was with the Laboratory for Information and Decision Systems as well as the MIT-Harvard Neuroscience Statistics Research Laboratory. Her research interests include wearable technologies, medical cyber-physical systems, control, estimation, and system identification of biomedical and neural systems.

Dr. Faghih is the recipient of various awards including a 2023 National Institutes of Health (NIH) Maximizing Investigators' Research Award for Early Stage Investigators, an MIT Technology Review 2020 Innovator Under 35 award, a 2020 National Science Foundation (NSF) CAREER Award, a 2020 Research Excellence award as well as a 2020 Teaching Excellence Award from the University of Houston's Cullen College of Engineering, and the 2016 IEEE-USA New Face of Engineering award, a National Science Foundation Graduate Research Fellowship, an MIT Graduate Fellowship, and the University of Maryland's Department of Electrical and Computer Engineering Chair's Award. She was selected by the National Academy of Engineering for the 2019 US Frontiers of Engineering (FOE) Program and the 2023 EU-US FOE Program. In 2020, she was featured by the IEEE Women in Engineering Magazine as a "Woman to Watch". Dr. Faghih is on the editorial board of PNAS Nexus by the National Academy of Sciences and IEEE Transactions on Neural Systems and Rehabilitation Engineering. Dr. Faghih is a senior member of IEEE and has also been inducted into various honor societies including Phi Kappa Phi, Tau Beta Pi, and Eta Kappa Nu. In 2022, she was inducted into the University of Maryland's A. James Clark School of Engineering's Early Career Distinguished Alumni Society.

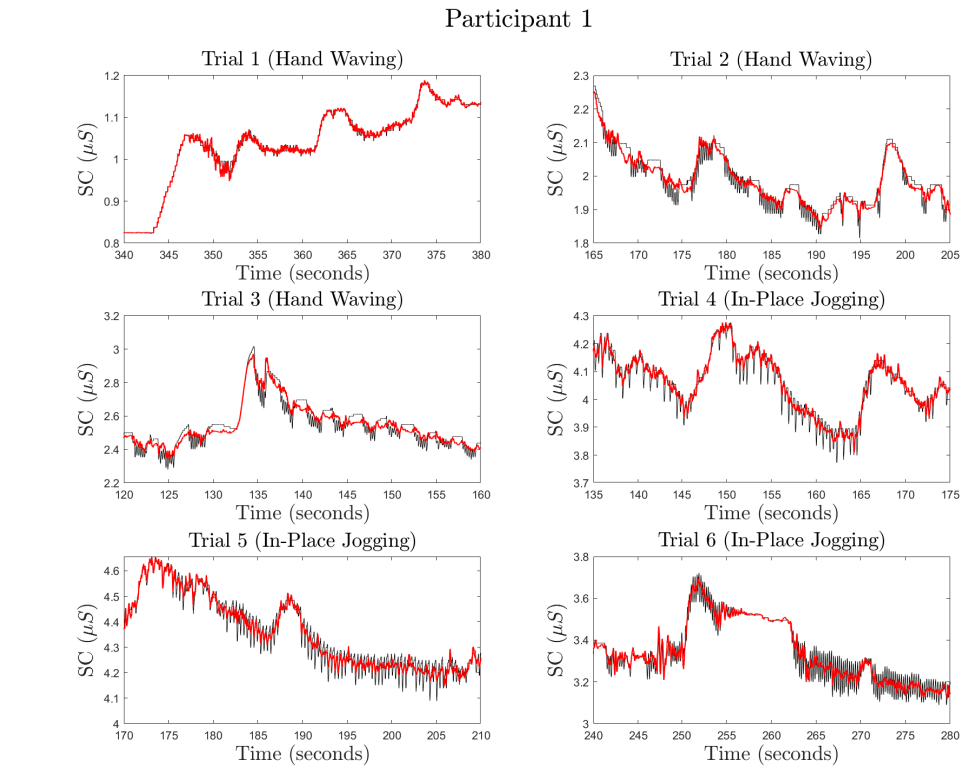

(a)

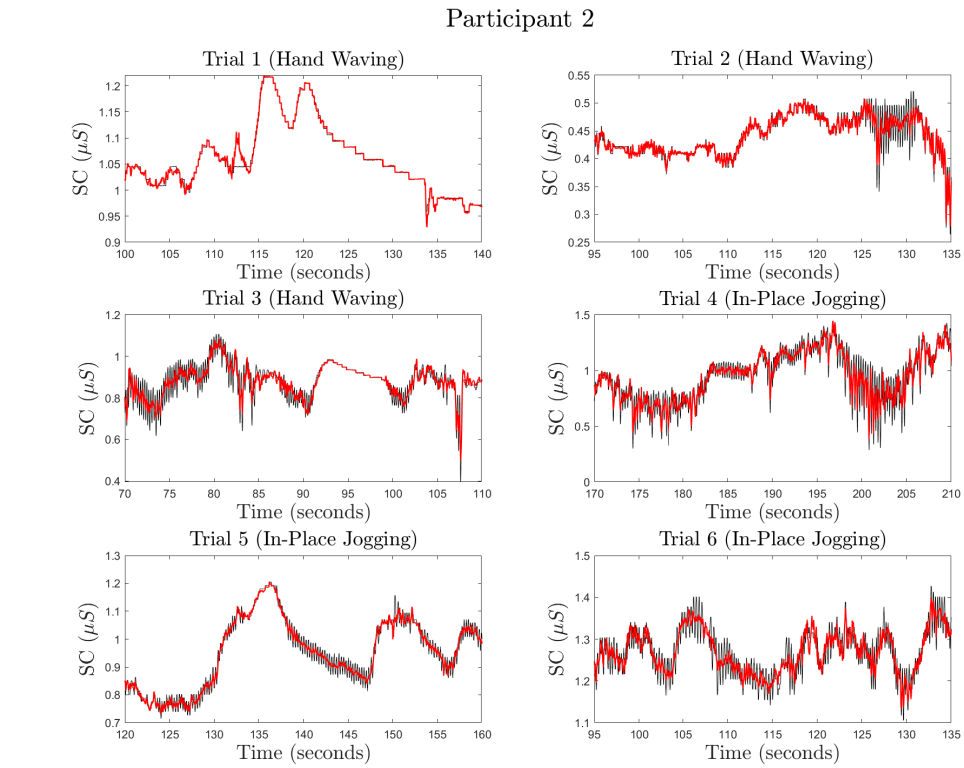

(b)

FIGURE 5: **Closer View of Different Segments of the Motion Reduced Results for All Trials from Both Participants.** Each panels in subplot (a) and (b) denotes a zoomed in plots different segments from Participant 1 and 2. Black and red lines denote the raw SC data and artifact reduced SC data.

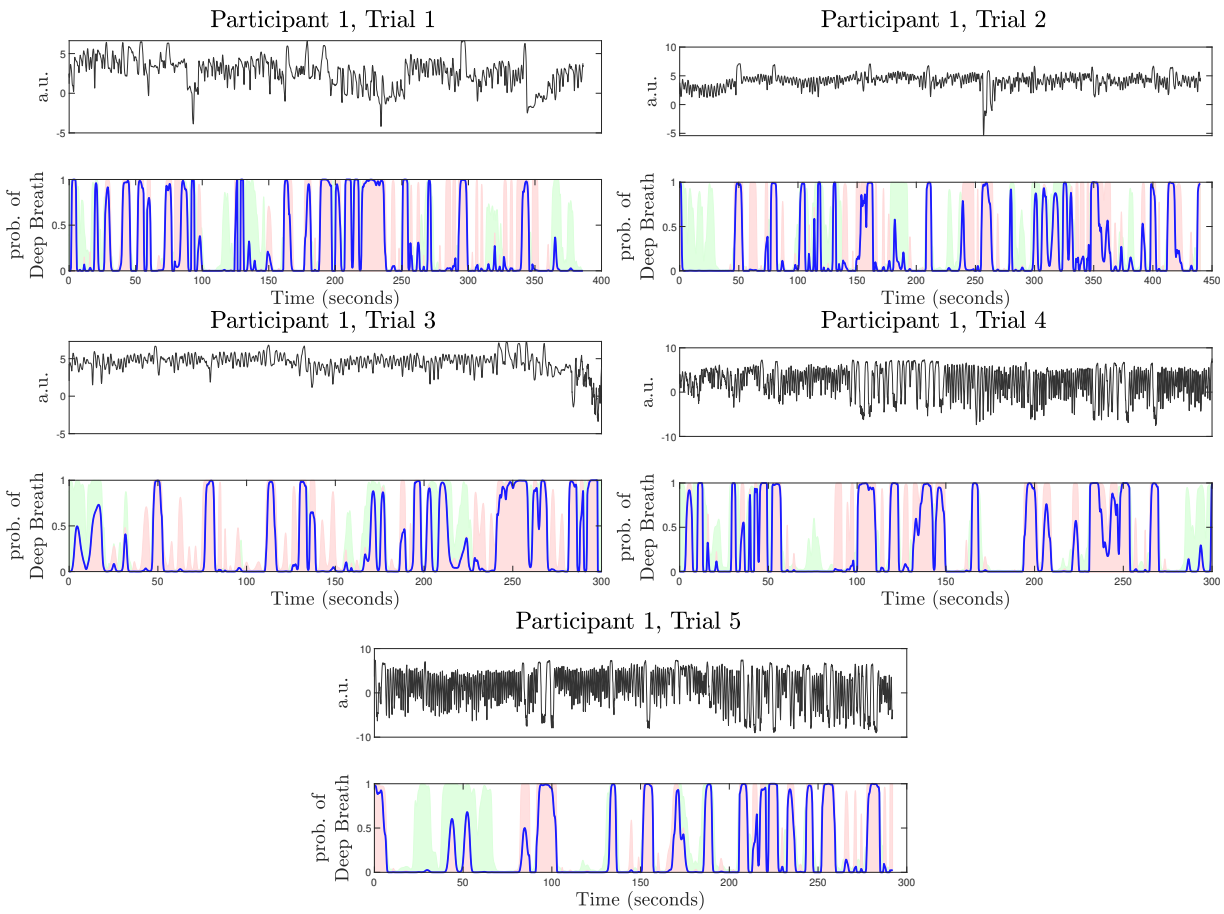

FIGURE 6: **Deep Breath Detection Results for Five Trials of Participant 1.** In each panel, the top subplot denotes the raw respiration signal recorded from the respiration belt, the bottom subplot shows the estimated detection probability $p[k]$ (blue lines). The light red and green shaded region represent the intermediate probabilities $p_1[k]$ and $p_2[k]$, respectively.

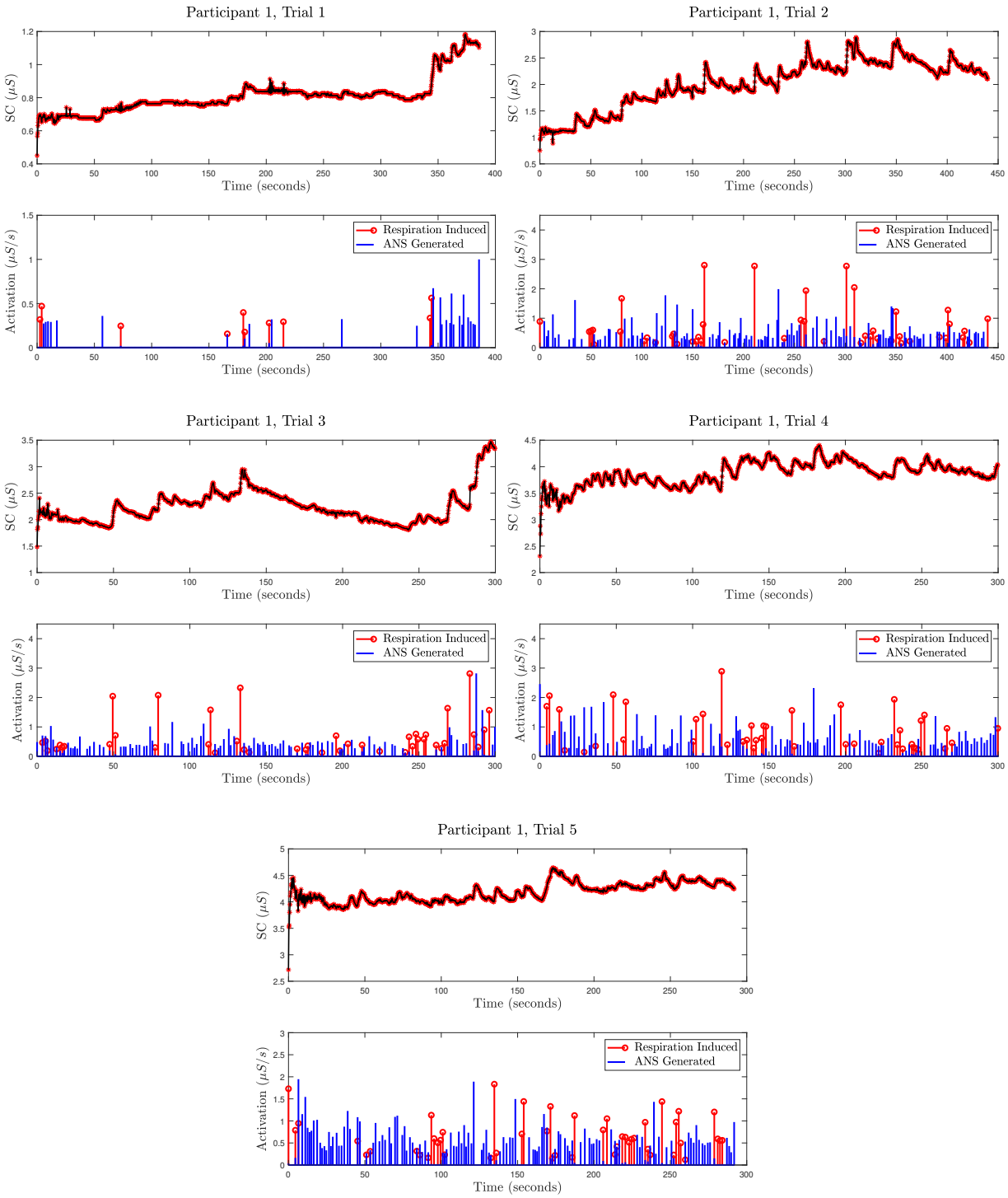

FIGURE 7: **Separation of Respiration Induced Electrodermal Activity from the Inferred ANS Activation for Five Trials from Participant 1.** In each panel, the top subplot denotes the artifact reduced (red stars) and the reconstructed SC (black lines), the bottom subplot shows the separated respiration induced activation and the pure ANS generated activation.

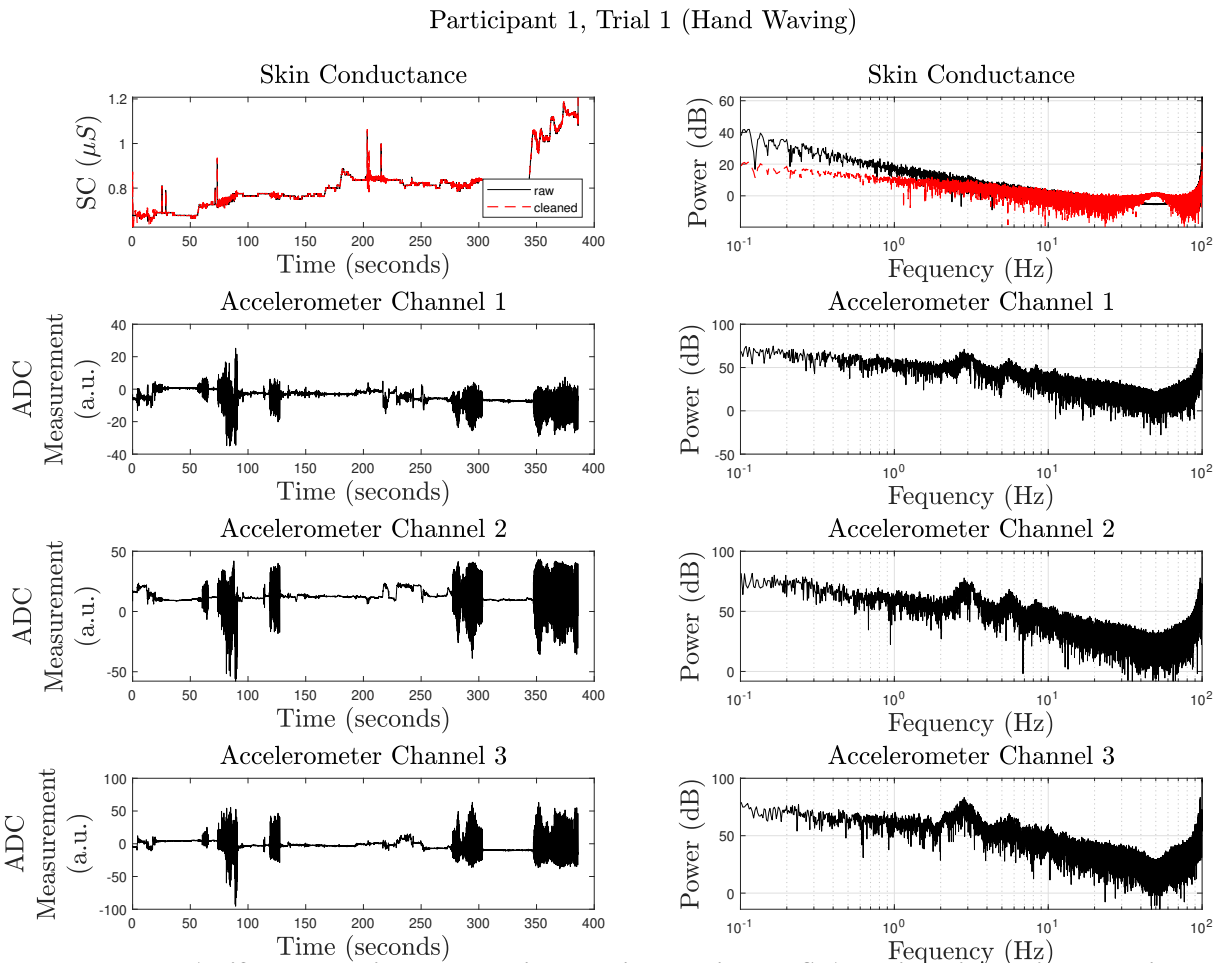

FIGURE 8: **Example Artifact Reduction Result with Multi-resolution RLS Adaptive Filter with Experimental SC Recording from Participant 1, Trial 1, During Hand Waving.** The first left panel depicts raw (artifact corrupted) and cleaned (artifact reduced) SC data. The first right panel shows the corresponding power spectrum density. The next three panels show three accelerometer channel recordings on the left and their corresponding power spectrum density on the right.

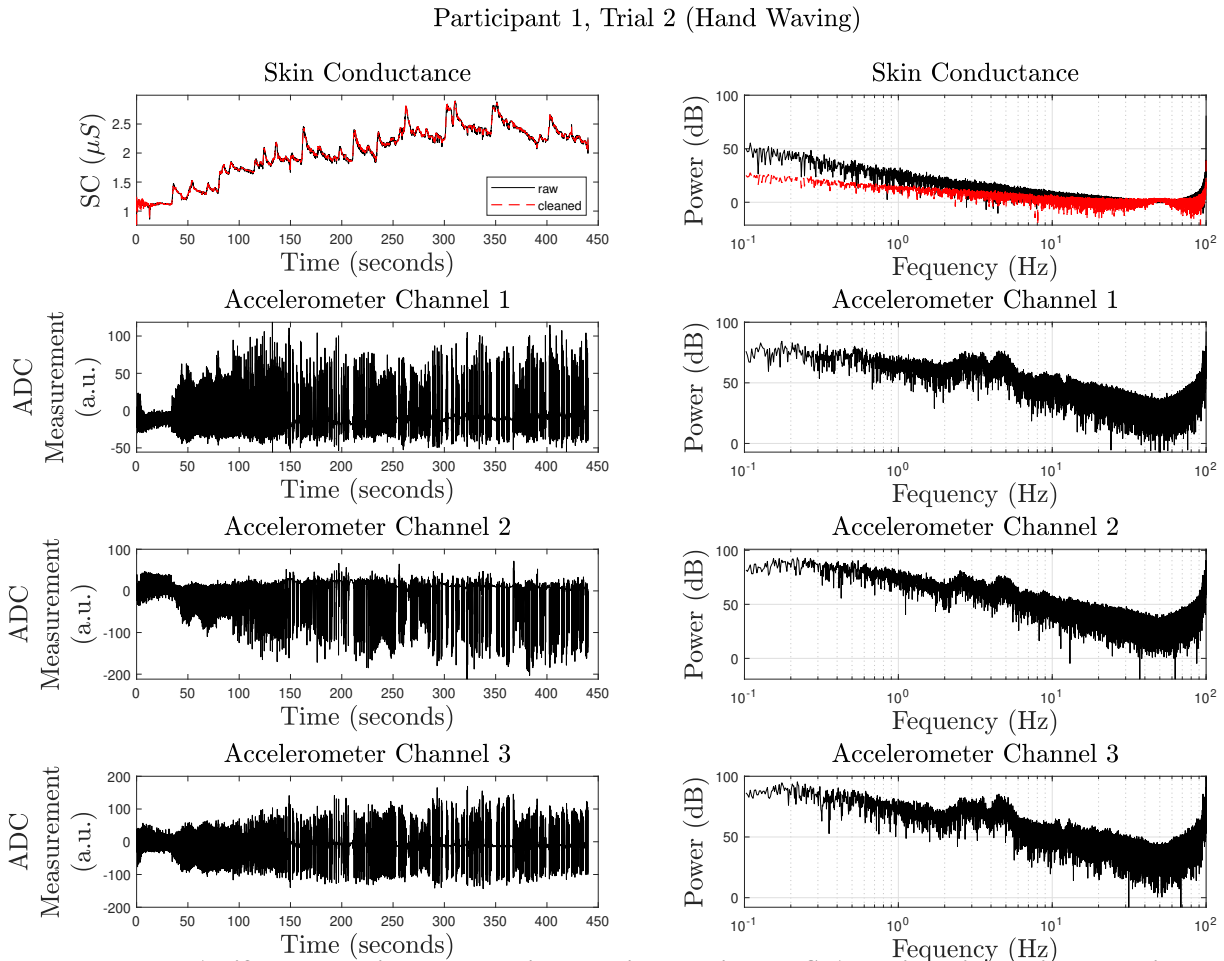

FIGURE 9: **Example Artifact Reduction Result with Multi-resolution RLS Adaptive Filter with Experimental SC Recording from Participant 1, Trial 2, During Hand Waving.** The first left panel depicts raw (artifact corrupted) and cleaned (artifact reduced) SC data. The first right panel shows the corresponding power spectrum density. The next three panels show three accelerometer channel recordings on the left and their corresponding power spectrum density on the right.

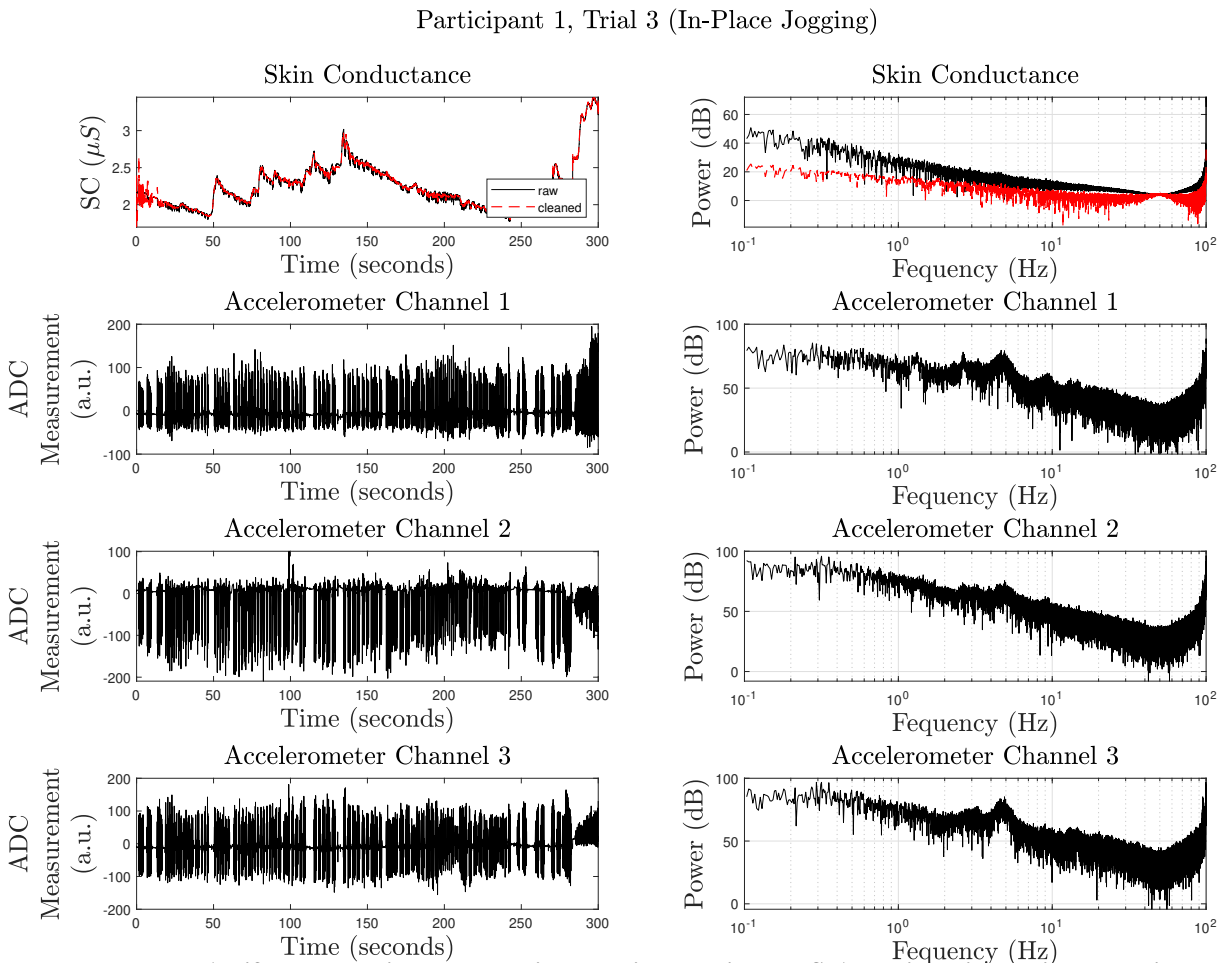

FIGURE 10: **Example Artifact Reduction Result with Multi-resolution RLS Adaptive Filter with Experimental SC Recording from Participant 1, Trial 3, During Hand Waving.** The first left panel depicts raw (artifact corrupted) and cleaned (artifact reduced) SC data. The first right panel shows the corresponding power spectrum density. The next three panels show three accelerometer channel recordings on the left and their corresponding power spectrum density on the right.

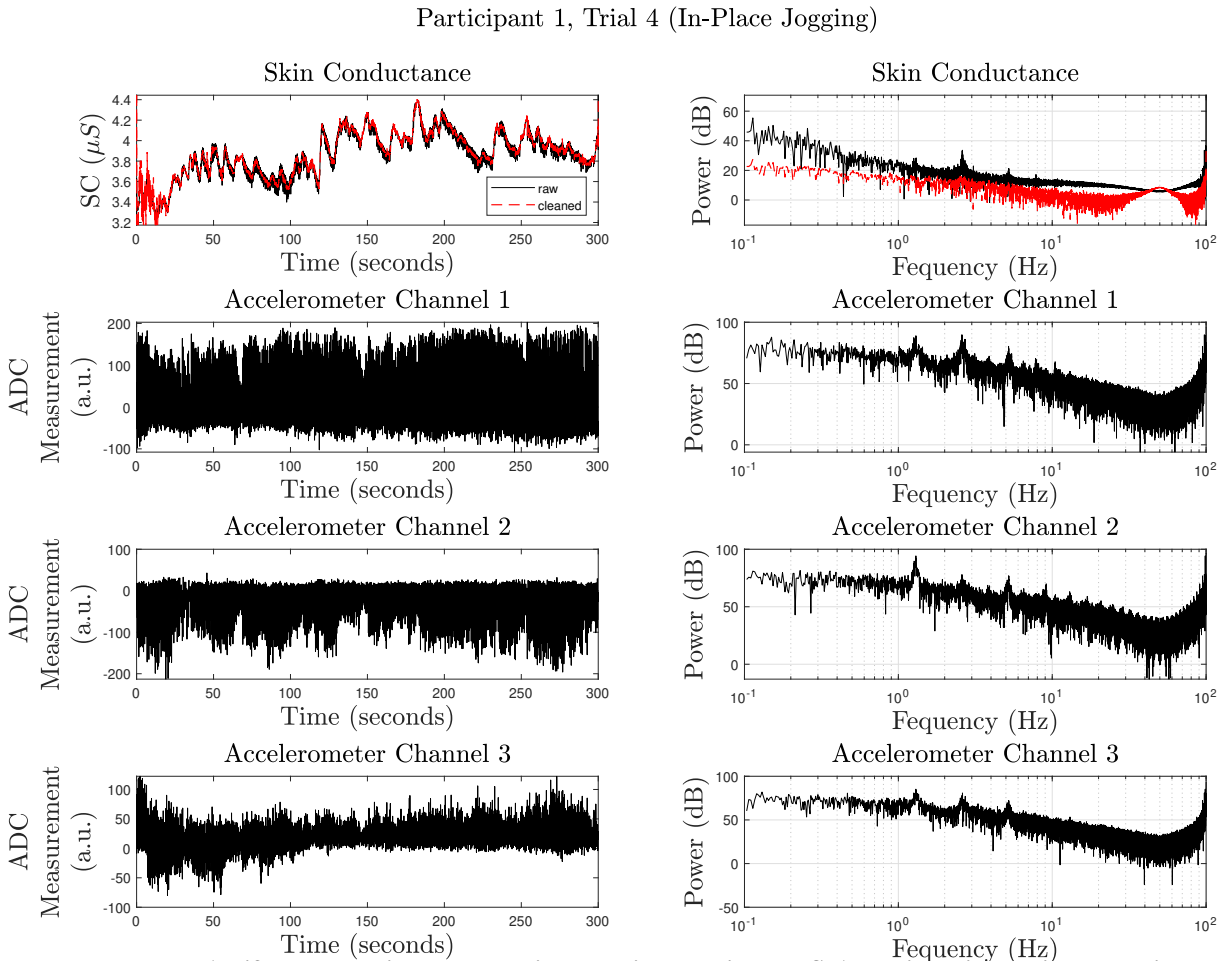

FIGURE 11: **Example Artifact Reduction Result with Multi-resolution RLS Adaptive Filter with Experimental SC Recording from Participant 1, Trial 4 During, Hand Waving.** The first left panel depicts raw (artifact corrupted) and cleaned (artifact reduced) SC data. The first right panel shows the corresponding power spectrum density. The next three panels show three accelerometer channel recordings on the left and their corresponding power spectrum density on the right.

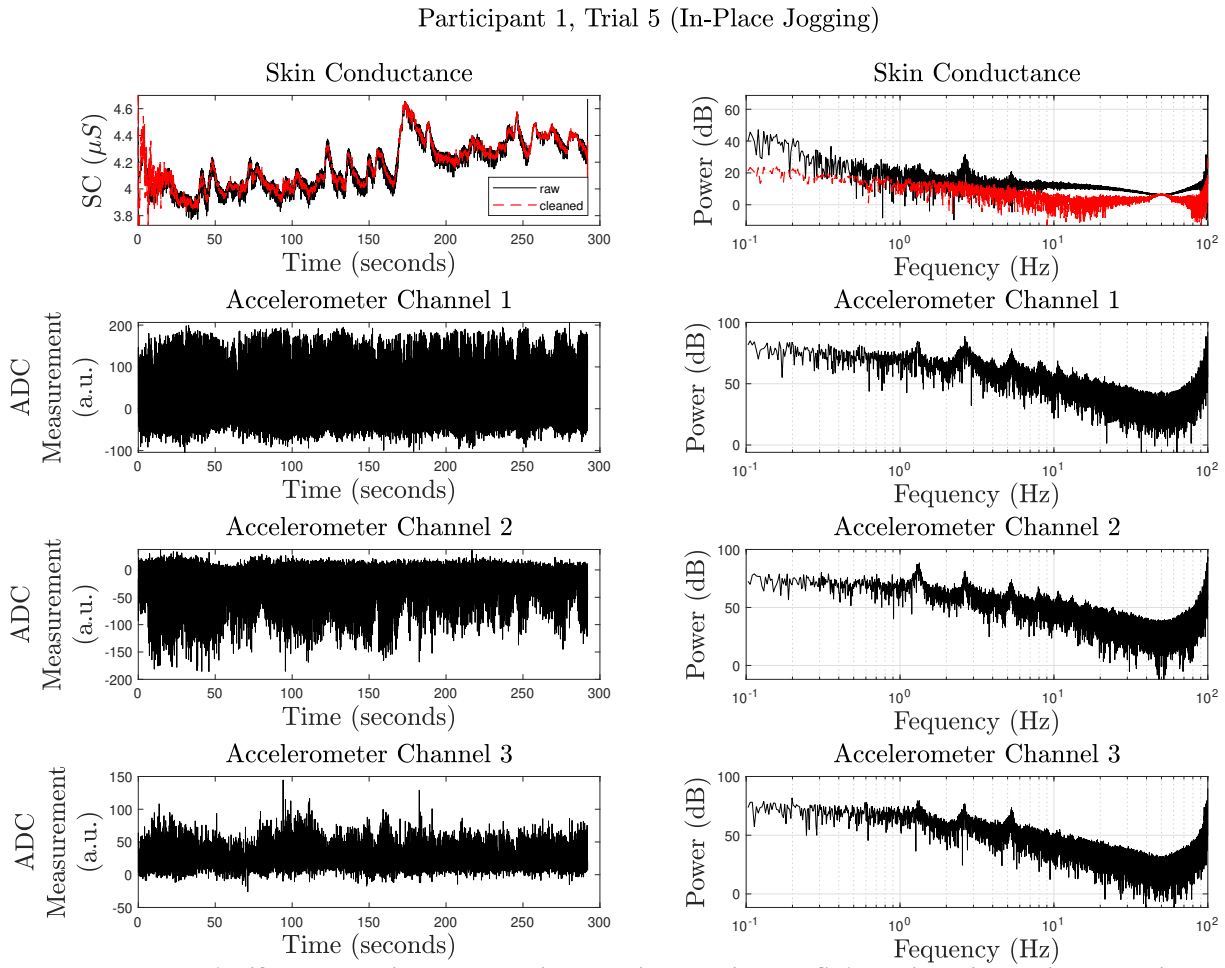

FIGURE 12: **Example Artifact Reduction Result with Multi-resolution RLS Adaptive Filter with Experimental SC Recording From Participant 1, Trial 5, During Hand Waving.** The first left panel depicts raw (artifact corrupted) and cleaned (artifact reduced) SC data. The first right panel shows the corresponding power spectrum density. The next three panels show three accelerometer channel recordings on the left and their corresponding power spectrum density on the right.

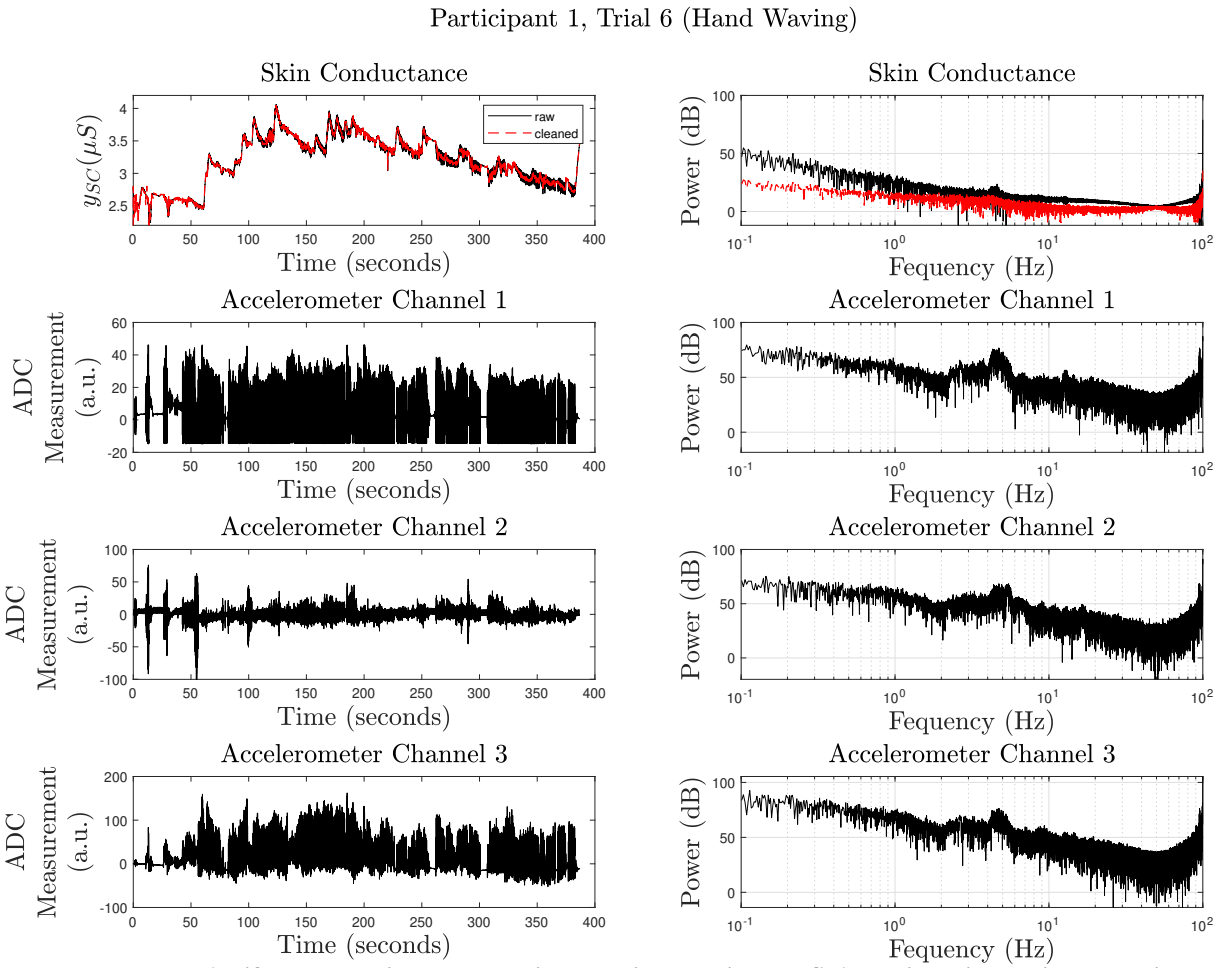

FIGURE 13: **Example Artifact Reduction Result with Multi-resolution RLS Adaptive Filter with Experimental SC Recording from Participant 1, Trial 6, During Hand Waving.** The first left panel depicts raw (artifact corrupted) and cleaned (artifact reduced) SC data. The first right panel shows the corresponding power spectrum density. The next three panels show three accelerometer channel recordings on the left and their corresponding power spectrum density on the right.

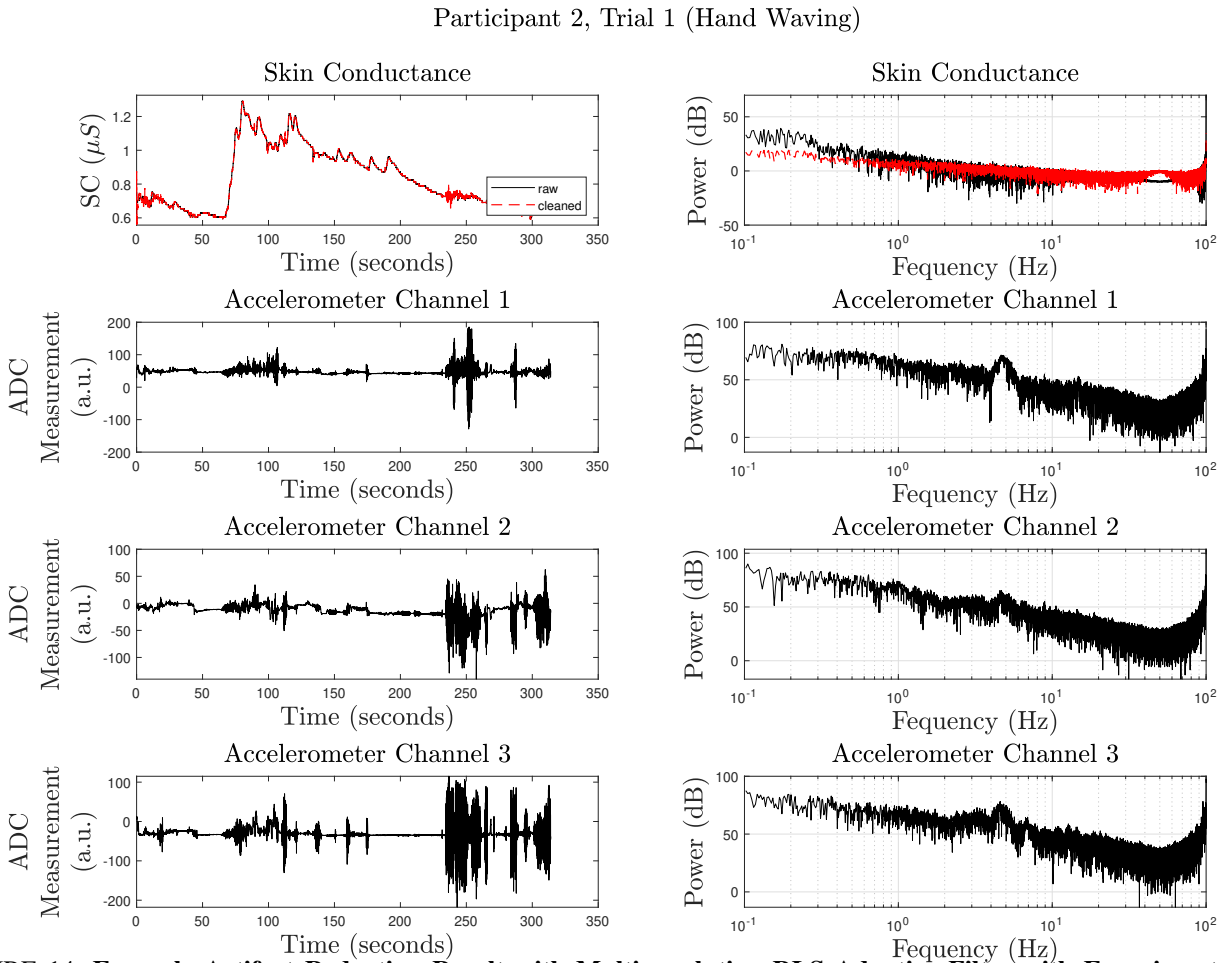

FIGURE 14: **Example Artifact Reduction Result with Multi-resolution RLS Adaptive Filter with Experimental SC Recording from Participant 2, Trial 1, During Hand Waving.** The first left panel depicts raw (artifact corrupted) and cleaned (artifact reduced) SC data. The first right panel shows the corresponding power spectrum density. The next three panels show three accelerometer channel recordings on the left and their corresponding power spectrum density on the right.

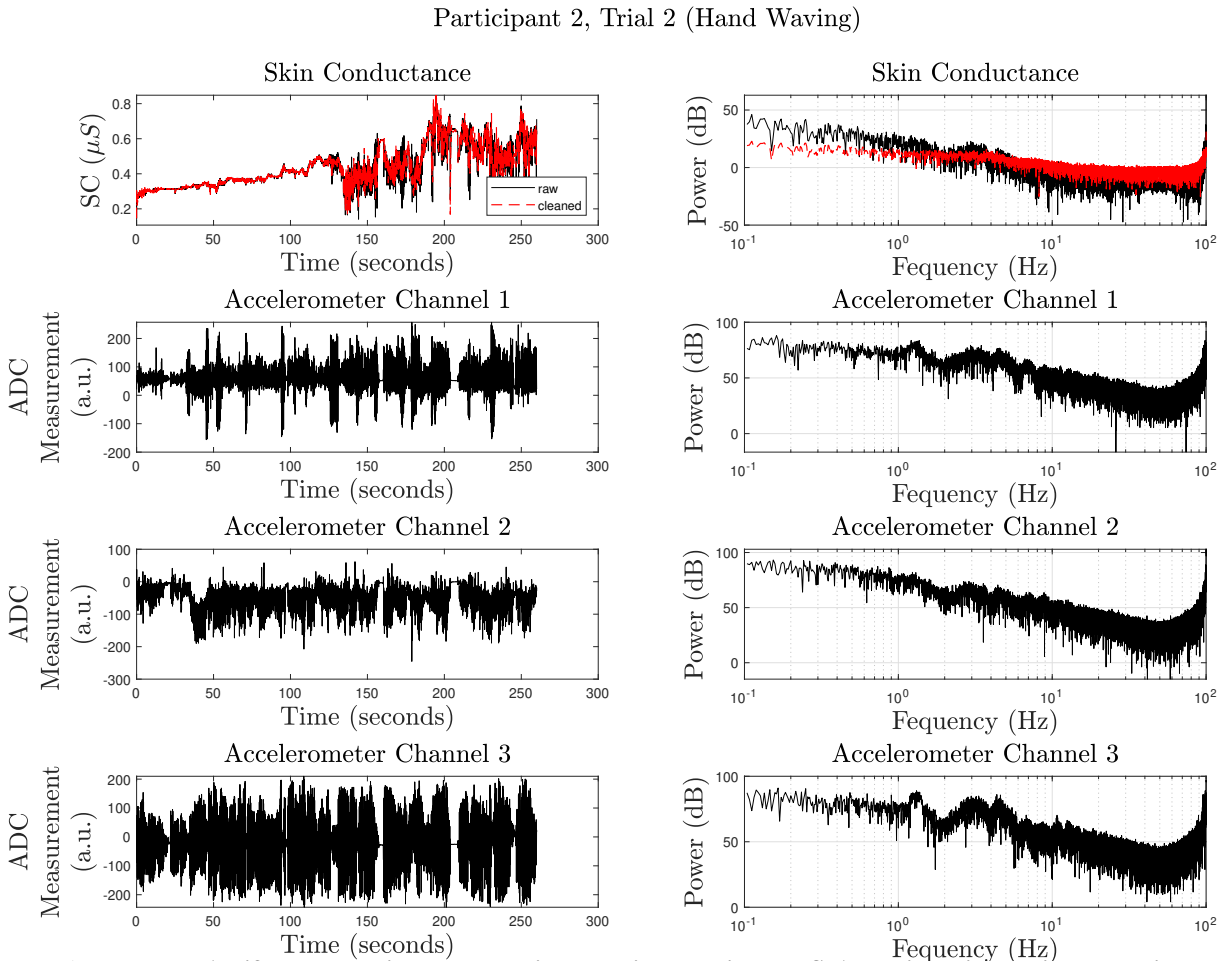

FIGURE 15: **Example Artifact Reduction Result with Multi-resolution RLS Adaptive Filter with Experimental SC Recording from Participant 2, Trial 2, During Hand Waving.** The first left panel depicts raw (artifact corrupted) and cleaned (artifact reduced) SC data. The first right panel shows the corresponding power spectrum density. The next three panels show three accelerometer channel recordings on the left and their corresponding power spectrum density on the right.

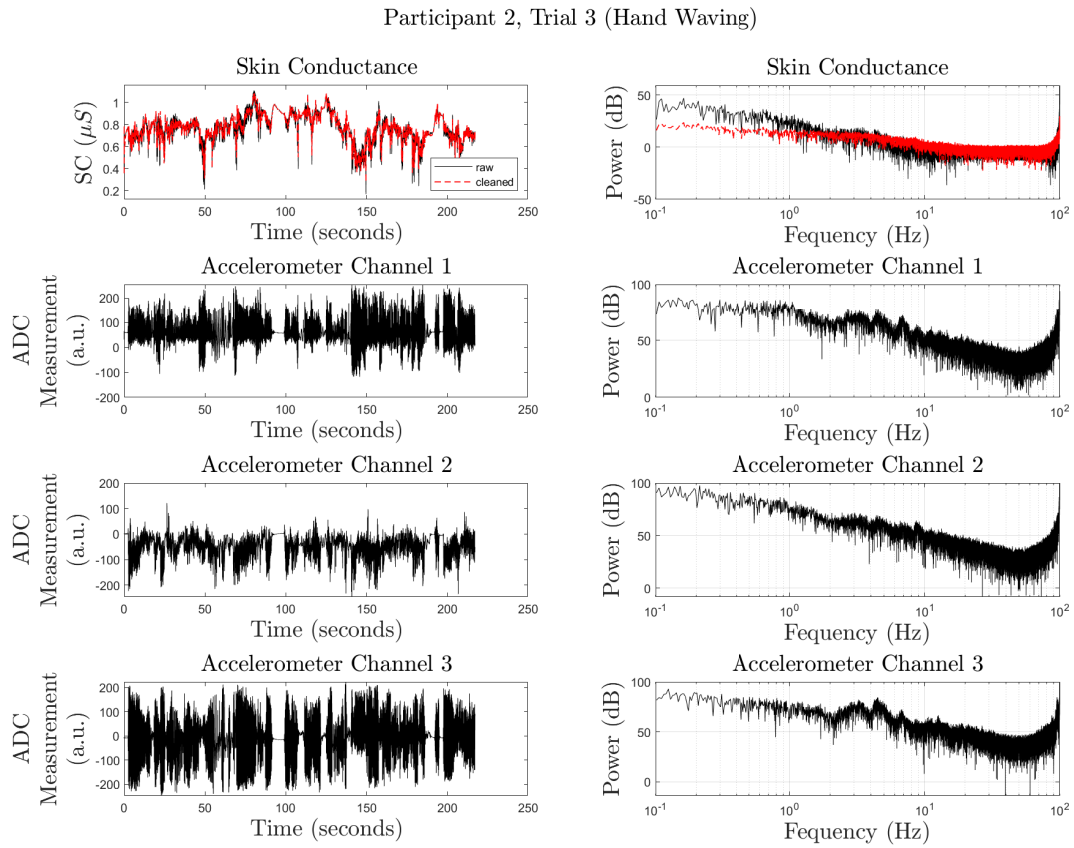

FIGURE 16: **Example Artifact Reduction Result with Multi-resolution RLS Adaptive Filter with Experimental SC Recording from Participant 2, Trial 3, During Hand Waving.** The first left panel depicts raw (artifact corrupted) and cleaned (artifact reduced) SC data. The first right panel shows the corresponding power spectrum density. The next three panels show three accelerometer channel recordings on the left and their corresponding power spectrum density on the right.

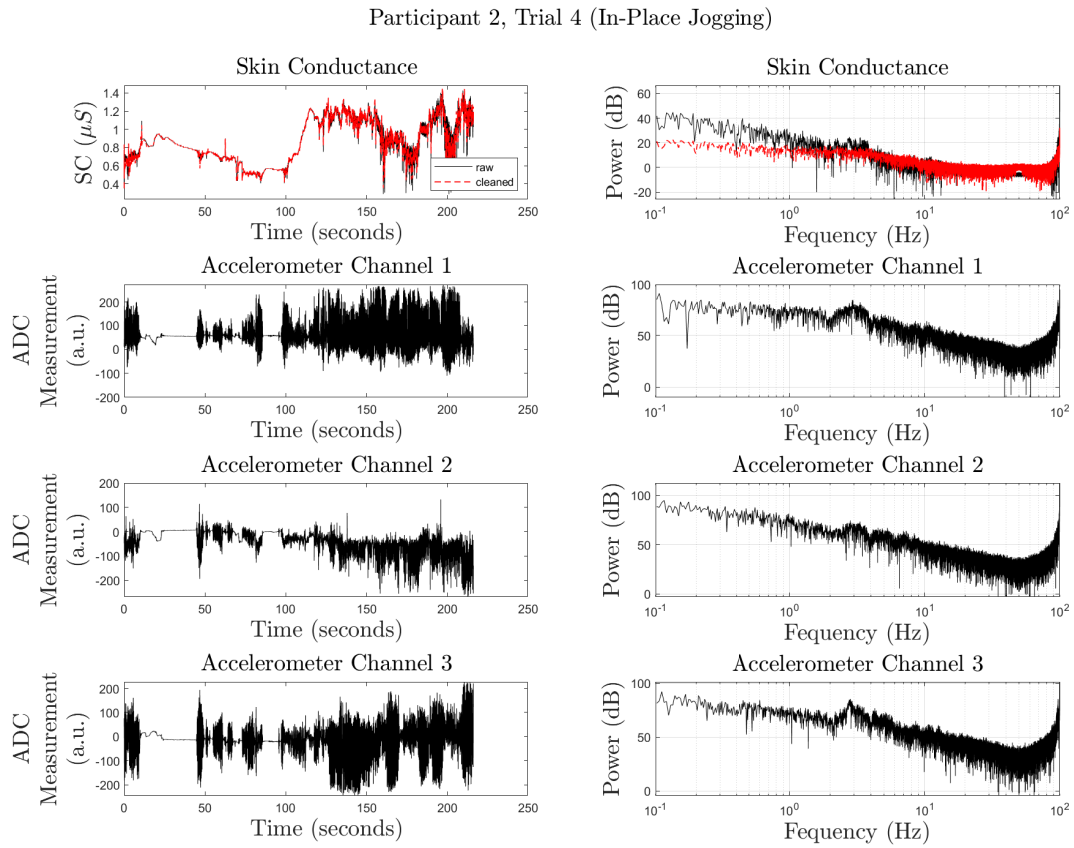

FIGURE 17: **Example Artifact Reduction Result with Multi-resolution RLS Adaptive Filter with Experimental SC Recording from Participant 2, Trial 4, During Hand Waving.** The first left panel depicts raw (artifact corrupted) and cleaned (artifact reduced) SC data. The first right panel shows the corresponding power spectrum density. The next three panels show three accelerometer channel recordings on the left and their corresponding power spectrum density on the right.

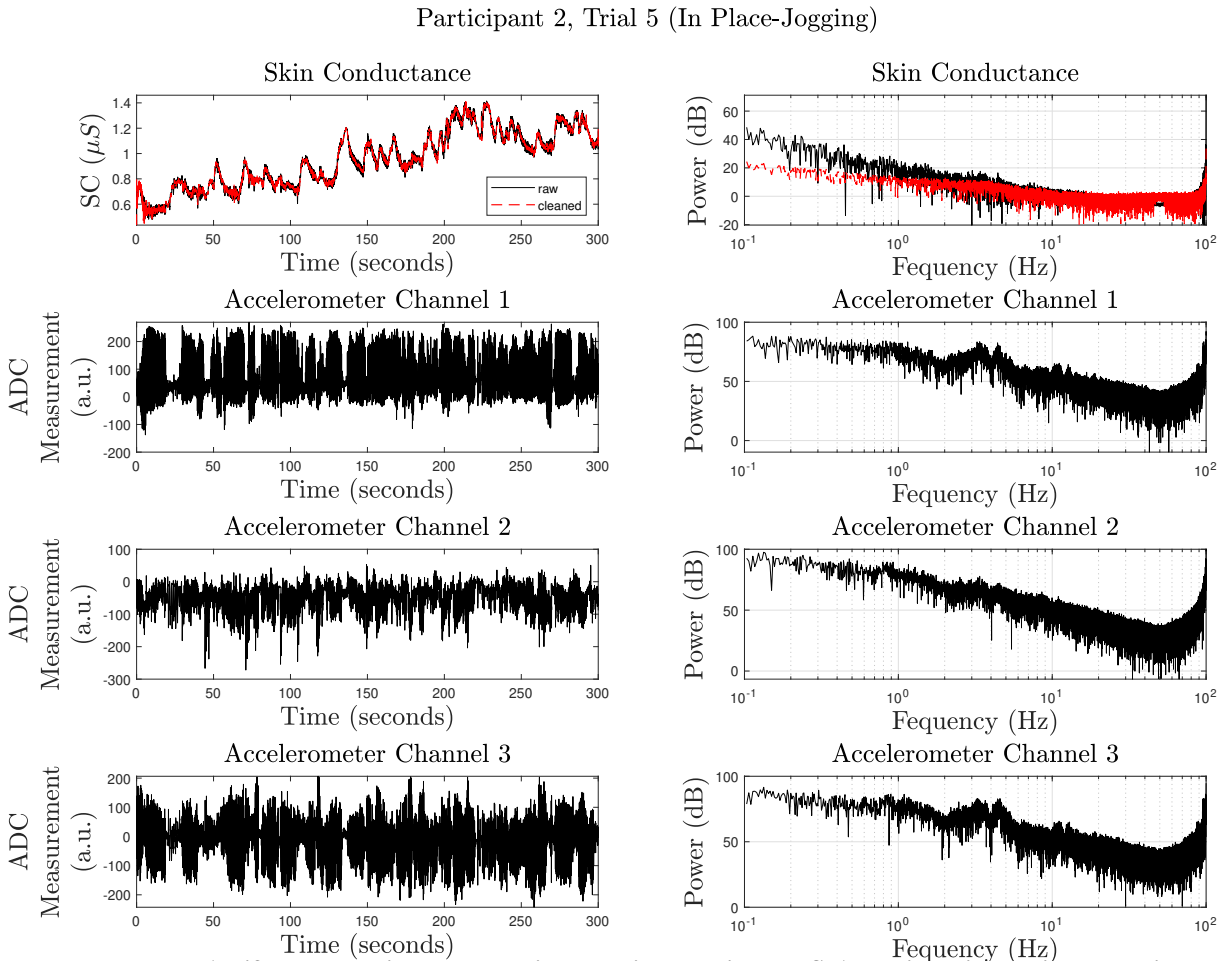

FIGURE 18: **Example Artifact Reduction Result with Multi-resolution RLS Adaptive Filter with Experimental SC Recording from Participant 2, Trial 5, During Hand Waving.** The first left panel depicts raw (artifact corrupted) and cleaned (artifact reduced) SC data. The first right panel shows the corresponding power spectrum density. The next three panels show three accelerometer channel recordings on the left and their corresponding power spectrum density on the right.

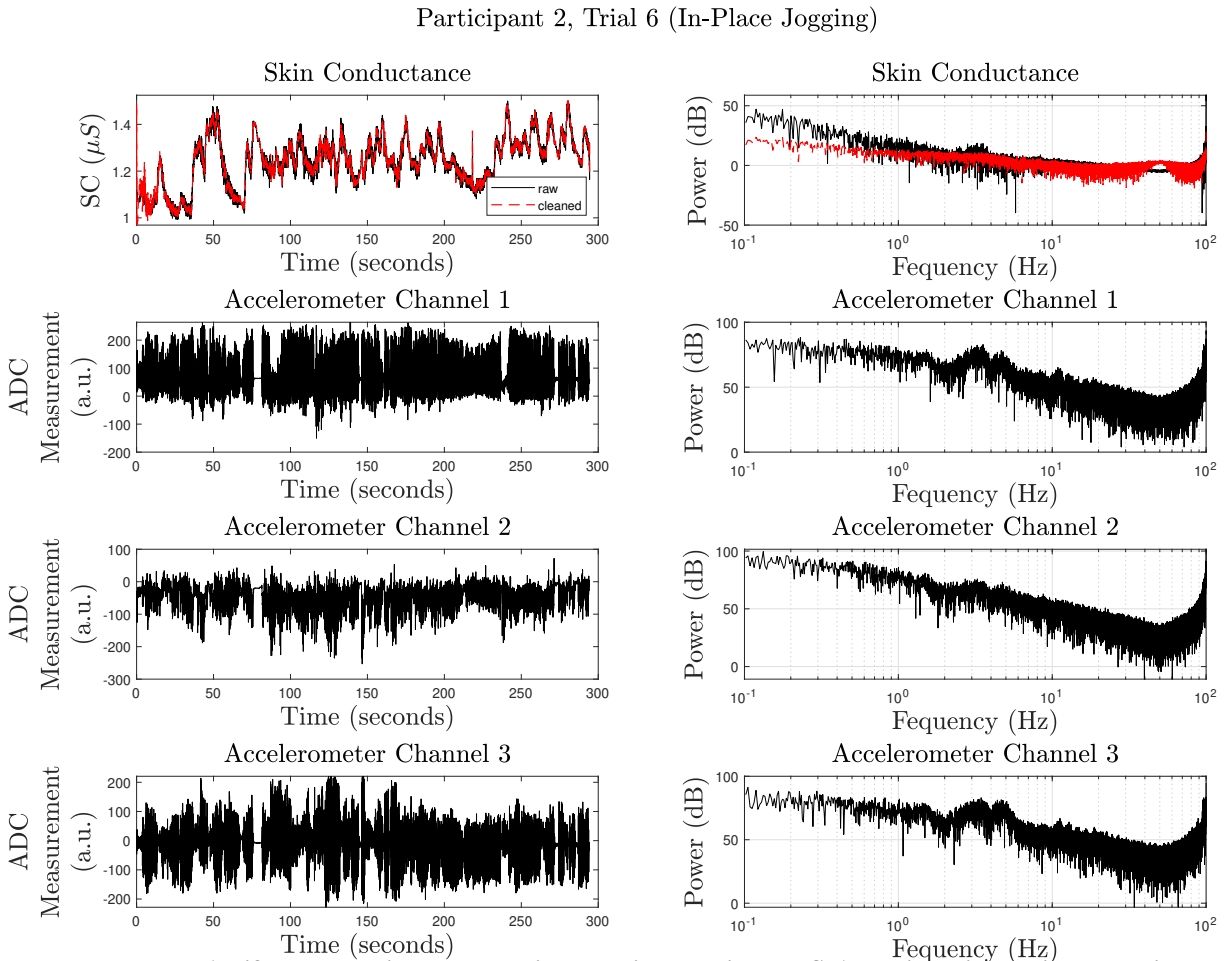

FIGURE 19: **Example Artifact Reduction Result with Multi-resolution RLS Adaptive Filter with Experimental SC Recording from Participant 2, Trial 6, During Hand Waving.** The first left panel depicts raw (artifact corrupted) and cleaned (artifact reduced) SC data. The first right panel shows the corresponding power spectrum density. The next three panels show three accelerometer channel recordings on the left and their corresponding power spectrum density on the right.